INL/EXT-14-32951
Revision 0

Initial Assessment of X-ray Computed Tomography Image Analysis for Material Defect Microstructure

Joshua J. Kane
William E. Windes

June 2016

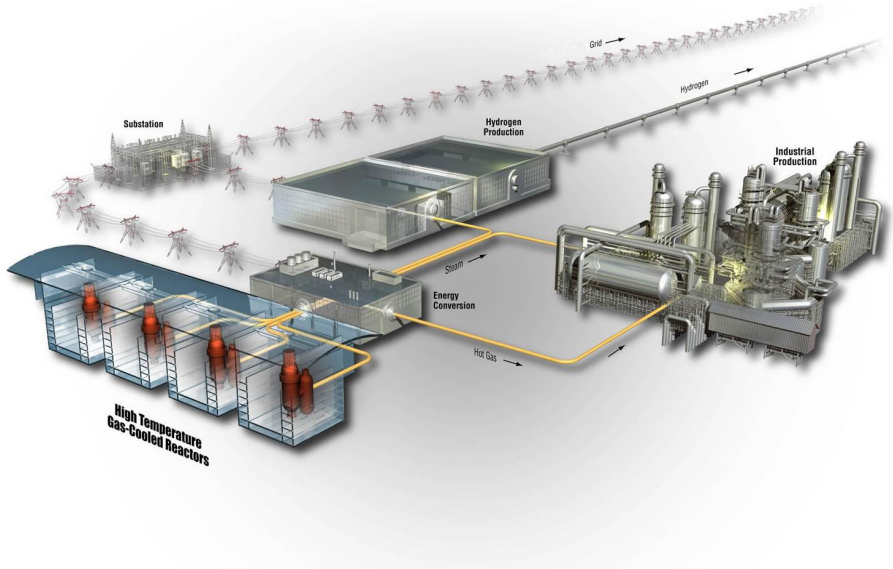

The INL is a
U.S. Department of Energy
National Laboratory
operated by
Battelle Energy Alliance

Idaho National Laboratory

INL/EXT-14-32951
Revision 0

Initial Assessment of X-ray Computed Tomography Image Analysis for Material Defect Microstructure

Joshua J. Kane
William E. Windes

June 2016

Idaho National Laboratory
ART Graphite Program
Idaho Falls, Idaho 83415

http://www.inl.gov

Prepared for the
U.S. Department of Energy
Office of Nuclear Energy
Under DOE Idaho Operations Office
Contract DE-AC07-05ID14517

INL ART TDO Program

Initial Assessment of X-ray Computed Tomography Image Analysis for Material Defect Microstructure

INL/EXT-14-32951
Revision 0

June 2016

Authors:

Joshua J. Kane
Staff Scientist — 6/29/2016 Date

Technical Reviewer: (Confirmation of mathematical accuracy, and correctness of data and appropriateness of assumptions.)

William Windes
INL ART Graphite R&D Technical Lead — 6/29/2016 Date

Approved by:

Michael E. Davenport
Project Manager — 6/29/16 Date

Diane V. Croson
INL ART TDO Deputy Director — 6/29/16 Date

Michelle T. Sharp
INL ART TDO Quality Assurance — 6/29/16 Date

SUMMARY

The original development work leading to this report was focused on the non-destructive three-dimensional (3-D) characterization of nuclear graphite as a means to better understand the nature of the inherent pore structure. The pore structure of graphite and its evolution under various environmental factors such as irradiation, mechanical stress, and oxidation plays an important role in their observed properties and characteristics. In order for graphite research to transition from an empirical understanding of graphite behavior to a predictive mechanistic understanding, the pore structure must be well characterized and understood. As the pore structure within nuclear graphite is highly interconnected and truly 3-D in nature, 3-D characterization techniques are critical.

While 3-D characterization has been an excellent tool for graphite pore characterization, it has also been applied with success to a broad number of materials systems over many length scales. Given the wide range of applications and the highly quantitative nature of the tool, it is quite surprising to discover how infrequently this analysis is used in nuclear material research.

The report is divided into three main sections. The first section introduces the potential usefulness of 3-D image analysis in materials characterization. Section 2 provides an overview of some of the key principals and concepts needed to extract a wide variety of quantitative metrics from a 3-D representation of a material microstructure. The discussion includes a brief overview of segmentation methods, connective components, morphological operations, distance transforms, and skeletonization.

Section 3 focuses on the application of concepts from Section 2 to relevant materials research at Idaho National Laboratory. In this section, detailed microstructural features within a variety of material (nuclear graphite, TREAT low-enriched uranium conversion program, and tristructural isotropic fuel particles) are resolved using quantitative methods described in Section 2. Different materials have been used other than nuclear graphite to demonstrate the potential in identifying a range of microstructure features and to provide a broad perspective of the applicability of quantitative image analysis to relevant materials of interest.

ACKNOWLEDGEMENTS

In its infancy, this material was supported by the Department of Energy (National Nuclear Security Administration) under Award Nos. 00041394/00026 and DE-NE0000140 under the guidance and direction of Dr. Darryl P. Butt from Boise State University's Materials Science and Engineering Department. Current development has occurred at Idaho National Laboratory under funding from the DOE-NE Advanced Reactor Technology (ART) program and the National Nuclear Security Administration's (NNSA) Office of Material Management and Minimization Reactor Conversion Program.

Dr. Elisa Barney Smith from Boise State University's Electrical and Computer Engineering Department was also instrumental in the development of this material. She provided detailed discussion with the authors regarding several principles and concepts discussed in the report. Many of these discussions impacted the content of the principles and concepts section.

CONTENTS

FIGURES

ACRONYMS

AGR	Advanced Gas Reactor
ART	Advanced Reactor Technology
CT	computed tomography
DOE	U.S. Department of Energy
HTR	High Temperature Reactor
INL	Idaho National Laboratory
LEU	low-enriched Uranium
ROI	Region of Interest
SEM	Scanning Electron Microscope
SiC	Silicon Carbide
TREAT	Transient Reactor Test Facility
TRISO	tristructural isotopic

Initial Assessment of X-ray Computed Tomography Image Analysis for Material Defect Microstructure

1. INTRODUCTION

Understanding the behavior of materials often begins with the ability to visualize its various levels of structure. Consequently, it is not surprising that imaging has and will play an essential role in the understanding of materials. While humans have examined objects under microscopes for centuries, the birth of modern image processing and analysis began in the early 1960s with the availability of computers powerful enough to carry out meaningful automated processing tasks. The first significant use of such processing was likely made by the Jet Propulsion Laboratory. Jet Propulsion Laboratory digitally processed pictures of the moon, taken by Ranger 7, to correct for known distortions in the on-board television camera.

Now, a little more than a half-century later, major leaps in computer performance and the widespread availability of personal computers have made image processing and analysis accessible to the vast majority of researchers. For example, many traditional (two-dimensional [2-D]) microscopy software programs come standard with some built-in processing and analysis capabilities to make measurements such as particle size, morphology, and volume fraction estimates of features and defects within a material. While such 2-D measurements can provide valuable insight, it is important to question the validity of measurements taken from a 2-D cross-section of a 3-D material can be. In short, assumptions have to be made regarding the shape and curvature of the 3-D objects outside the field of view. Even when the assumptions are fairly reasonable, the derived information must be used with caution. To illustrate, two relatively simple examples are given in Figures 1 and 2.

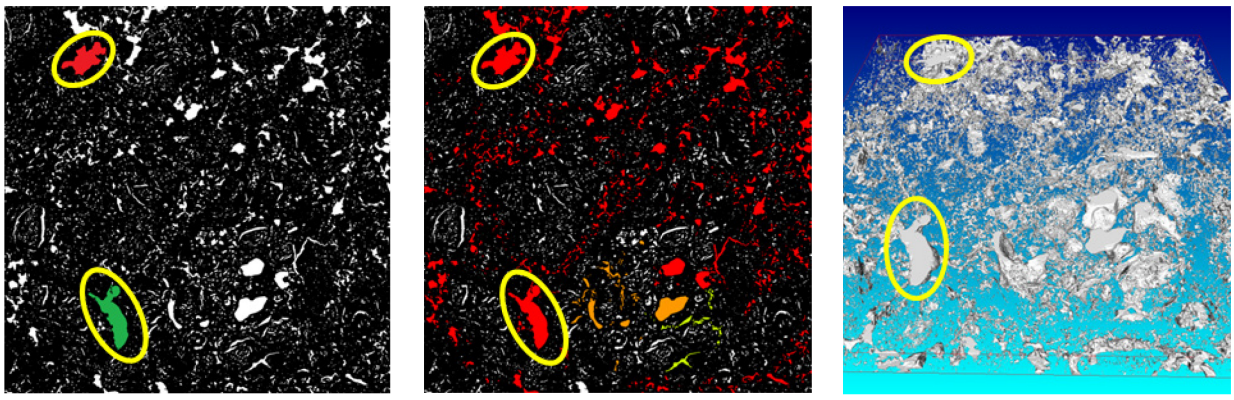

1a 1b 1c

Figure 1. 3-D image analysis - Example 1.

Figure 1 is an illustration to demonstrate the shortcomings of 2-D image processing and analysis of a 3-D structure. Figure 1a is a binary image of a graphite microstructure with two separate pores (defects) highlighted. Figure 1b is the same image, but uses 3-D image processing and analysis to group voxels into objects, thus illustrating that the “separate” pores are actually part of a larger interconnected defect pore structure rather than two separate pores as assumed in Figure 1a. Figure 1c is a 3-D volume subset of the pore structure demonstrating the interconnectivity as shown in Figure 1b.

As a first example, Figure 1 shows a binary image of NBG-18 graphite (SGL, Germany) derived from a single 2-D tomographic slice of a μX-ray computed tomography (CT) scan. NBG-18 is a candidate graphite for application in the next generation of high-temperature gas-cooled nuclear reactors. Two pores (defects) are highlighted in red and green, respectively. The two colored pores are assumed separate. While separating the pores, it is assumed both have only positive curvature with no re-entry angles. In other words, they are not connected. However, by interrogating the sample volumetrically, the assumption of positive curvature is shown to be false. The individual pores shown in Figure 1a are actually two branches of a large defect pore that runs across the entire length of the sample (Figures 1b and 1c).

The second example, Figure 2, illustrates a 2-D slice of a hypothetical microstructure containing 11 precipitates of a secondary phase. From Figure 2a, the precipitates appear to exhibit elliptical morphology and consequently inferences can be made regarding the size and aspect ratio of the precipitates; however, the precipitates are not elliptical at all. Examination of the same microstructure in 3-D reveals that the precipitates are actually right cylinders dispersed throughout the primary phase with small degrees of misalignment from the vertical direction of Figure 2b.

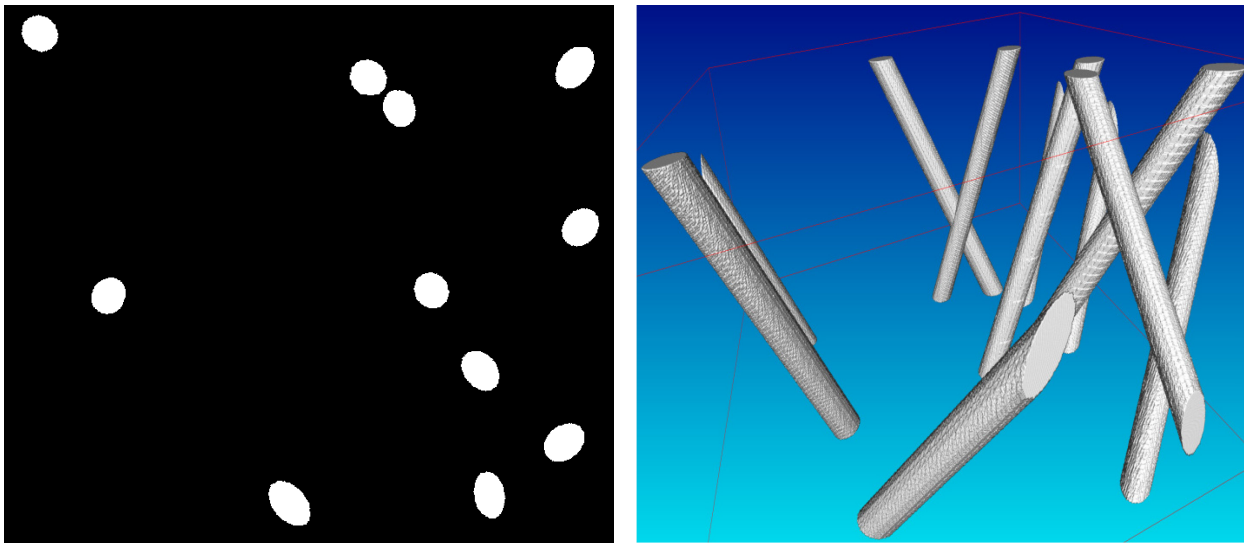

2a 2b

Figure 2. 3-D image processing - Example 2.

Figure 2 is a synthetic example illustrating a shortcoming of 2-D image processing and analysis of a 3-D volume. Figure 2a is a cross section of the 3-D image shown in Figure 2b. All cylinders are right cylinders with the same diameter with various degrees of rotational misalignment. Figure 2b is the full 3-D volume of the synthetic material.

While 2-D imaging and analysis is relatively quick and simple, it is plagued with many limiting assumptions that make it difficult to understand the true 3-D nature of a material. Utilization of a 3-D dataset removes all of the restrictive assumptions needed in a 2-D quantitative analysis, thus 3-D analysis can be a powerful technique for the quantitative interrogation of structural features on a wide range of scales. Today, there are many microscopy and characterization techniques capable of producing volumetric datasets that can be analyzed with 3-D image analysis. Some examples include, X-ray CT, transmission electron microscope-based tomography, Local Electrode Atom Probe, serial sectioning via focused ion beam followed by automated image collection, and even 3-D Atomic Force Microscope tomography where the same probe used to examine the surface is also used to scrape it away layer by layer.

Until recently, many of these techniques were highly limited or impractical due to the size and computing time needed to make the desired calculations. Substantial increases in random access memory, multicore central processing units (and increase in their speed), as well as Graphics Processing Unit computing have increased the feasibility of performing these types of calculations on large dataset in reasonable time frames.

It should be noted that a majority of current 3-D volumetric data are used for only qualitative comparisons and informative analysis despite (1) powerful and non-restrictive quantitative analysis capabilities, (2) relatively easy access to tomographic instrumentation, and (3) available resources of modern computing. When quantitative analysis is applied to 3-D structures, the resulting data and conclusions regarding the material structures are exceptional.[1,2,3,4,5,6,7,8,9,10,11,12,13] *It is the **authors' shared opinion** that the underutilization of quantitative 3-D analysis for materials stems from a lack of knowledge by materials researchers regarding the basic tools and principles of image processing and analysis needed to achieve meaningful quantitative results.* This is quite understandable as many of the basic tools and principles are deeply rooted in computer and electrical engineering.

This report seeks to illustrate the potential of 3-D image analysis by providing a broad overview of some of the basic principles and concepts in image processing and analysis to a variety of materials. These principles and concepts will then be used to demonstrate the extraction of quantitative measurements from the microstructures of different materials characterized using μX-ray CT systems.

2. PRINCIPLES AND CONCEPTS

Image Analysis includes a wide range of principles and concepts. In this report, five primary subjects will be discussed briefly: Image Segmentation, Connective Components, Morphological Operations, Distance Transforms, and Skeletonization. Image segmentation and connective components are image processing techniques used to isolate the desired features in the image volume. The remaining three are tools for data manipulation that allow for extraction of meaningful geometric measurements within the microstructure from the volumetric data. This section pulls heavily from basic image processing and analyses texts, such as Gonzalez and Woods' textbook, "Digital Image Processing,"[14] and Soille's book, "Morphological Image Analysis Principles and Applications."[15] There are many texts available and the interested reader should examine references such as these for a more detailed description of the follow discussions.[16,17]

2.1 Segmentation

Segmentation in terms of 3-D material volumes can be defined as a subdivision of material into different regions of interest. This could imply simply dividing a solid into its constituent phases, isolating carbide precipitates from a metal alloy along a grain boundary, or even dividing a single-phase polycrystalline material into its individual grains. Hypothetically, any signal reconstructed in 3-D that provides spatial information about a material can be used for segmentation. Commonly the signal is directly related to density, chemical composition, or crystallographic orientation.

Image segmentation is often the most challenging hurdle to overcome in attempting to extract quantitative information from a material. If an accurate segmentation of the object(s) of interest cannot be achieved, the quantitative information obtained will have little-to-no real value. A plethora of algorithms and methodologies exist for separating features within images. It is not the intent of this report to comprehensively cover this subject; rather, a concise overview with examples will be given to leave the reader with an understanding of some basic methodologies to build upon.

2.1.1 Global Thresholds

Thresholding is arguably the easiest and most commonly used method in image segmentation. It is easily implemented when the intensity of the features of interest vary significantly from the background, Figure 3. Thresholding is often performed globally over the entire image (Figures 3a and 3b). When the

intensity of the region of interest (ROI) or the background does not vary significantly, a global threshold is easily determined (Figure 3a–3c). In real material microstructure systems, noise and variation within the ROI can make global thresholding more difficult. For example, Figure 3d is identical to Figure 3c with the exception of Gaussian white noise that has been added randomly to each pixel. This produces a final segmentation image that is not ideally clean and crisp, Figure 3e. The issue for this global segmentation is that intensity ranges of the various features overlap each other. When an intensity threshold is set, some pixels will be classified incorrectly as members of the incorrect ROI. While this is inevitable, additional processing steps, including filtration and morphological operations, can be used to "clean up" the image to better approximate the ideal image.

The global threshold can easily be set manually; however, in doing so, user bias can become an appreciable factor in the final outcome. A simple automated method for choosing a global threshold is known as Otsu's method. In Otsu's method, the intensity of each region of interest is assumed to be Gaussian in nature. At each possible threshold value (for example, 0-255 for an 8-bit gray scale image), integer binning of intensity values is used to calculate the class conditional distribution. The threshold value that maximizes the variance of the system is chosen to be the optimum threshold. This corresponds roughly with the local minimum between intensity peaks. Otsu's method can also be used to optimize multiple thresholds when features of interest vary in intensity (Figure 3f).

3a

3b

3c

3d

3e

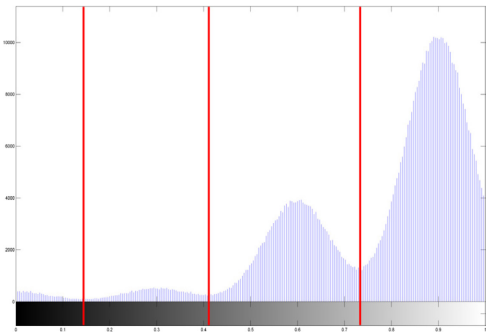

3f

Figure 3. Global thresholding.

Figure 3 contains examples of Otsu's method applied to various modified forms of the Idaho National Laboratory (INL) logo. Figure 3a contains an original gray-scale image of the INL logo. Figure 3b is a binary image resulting from the application of Otsu's method to Figure 3a. Figure 3c is the INL logo with four levels of intensity to simulate multiple ROI. Figure 3d is the same image as Figure 3c with Gaussian noise added to the image. Figure 3e is the result of applying Otsu's method to Figure 3c using three global thresholds. Figure 3f is the gray-scale intensity histogram corresponding to Figure 3d. The three red lines indicate the "ideal" threshold values determined via Otsu's method for the three global thresholds.

2.1.2 Local Adaptive Thresholds

A global threshold method such as Otsu's method breaks down when there is a significant local variation in image intensity (Figures 4a and 4b). To handle spatially varying intensities, methods such as locally adaptive thresholds have been developed. In these methods, threshold criteria are based on information contained within a local kernel, rather than the entire image. Some simple local adaptive thresholding techniques include a moving average and multivariable thresholds based on the sample kernel's mean and standard deviation.

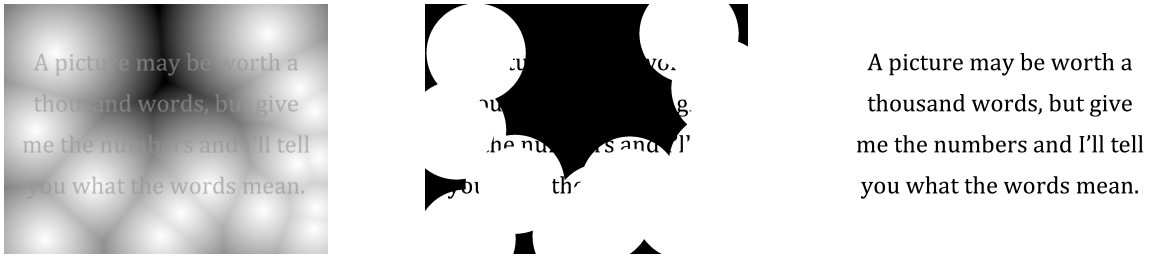

4a 4b 4c

Figure 4. Local adaptive threshold.

Figure 4 demonstrates the shortcomings of global thresholding in the presence of significant local variation in image intensity and the ability of local adaptive methods to overcome such issues. Figure 4a contains alpha-numeric characters embedded within an image with significant local variation in intensity. Figure 4b is a binary image resulting from application of a global threshold (determined via Otsu's method) to Figure 4a. Figure 4c is the result of a Sauvola local adaptive threshold algorithm applied to Figure 4a illustrating the ability of locally adaptive threshold techniques to differentiate between the image and alpha-numeric characters.

2.1.3 Texture Based Segmentation

Intensity may not always be an appropriate distinguishing feature for image segmentation in some materials applications (for instance, an examination of coarse pearlite microconstituents in steel). In such cases, it is the local texture of the image that should be used for segmentation. Many of the methods used for texture segmentation are based on statistical/entropic/anisotropic approaches to describing differences in the image. Basic segmentation methods include using the local standard deviation for segmentation rather than intensity, averaging of horizontal and vertical discrete cosine transform coefficients, and the use of morphological filters of varying sizes.

An example of texture based segmentation is demonstrated in Figure 5. Figure 5a is an image composed of two different circle sizes arranged to roughly resemble the Boise State University logo. Small circles make up the "B," while the background is composed of larger circles. Intuitively, since Figure 5a is a binary image, a typical threshold method will not work, however, the size and spacing of the circles that make up the "B" are different from the background. This differentiation can be used for segmentation. In a simple illustrative case such as this, morphological operators (described in Section 2.3) can be used to isolate the

ROI from the background. The boundary of the ROI is outlined in red in Figure 5b and the ROI is shown as a segmented binary object in Figure 5c.

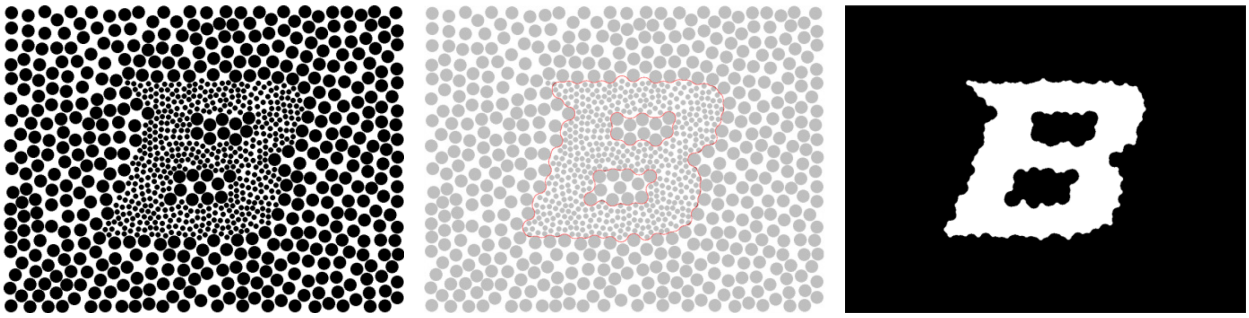

5a 5b 5c

Figure 5. Texture-based segmentation.

Figure 5 visually demonstrates texture-based segmentation. Figure 5a is an artificial textured image representing the Boise State University logo. The image is comprised of duplicates of two different circles. The diameters differ by a factor of approximately three. The red line in Figure 5b is used to indicate the boundary extracted between the two "phases" of different textures. Figure 5c is a binary image resulting from the texture-based segmentation to extract the Boise State University "B" from Figure 5a.

2.2 Connected Components

While most readers are probably familiar with a pixel and its 3-D equivalent, a voxel, it is important to briefly define their role in image analysis. In a 2-D image, a pixel is the smallest element within the image. Each pixel contains information representative of a small local area of the image. In photography, the pixel value is proportional to the intensity of light coming from that particular location of the image. While the signal detected varies from application to application, in all cases, pixels represent a spatial location and a detected response of that particular location to a probe. Voxels are the 3-D equivalent of pixels for 3-D images, representing the smallest volume element within the image. Similar to a pixel in photography, the voxel value can be interpreted to be representative of the intensity of the interrogation technique used to construct the 3-D image (i.e., X-ray intensity, Scanning Electron Microscope [SEM] electron intensity, or even individual atoms in Atom Probe Tomography).

Pixels (voxels) are most commonly represented as squares (cubes) because of the simplicity of the system and the ease of representing their coordinates with two (three) orthonormal vectors as the basis. Other shapes and coordinate systems can be used, but this leads to more complicated spatial calculations that limit the application of different shapes and coordinate systems to specialized applications.

In 2-D and 3-D image analysis of material microstructures, there is often more than one object to be characterized after segmentation. When more than one object exists, the question becomes how to define which pixels (voxels) are connected together so each object is recognized separately by the computational software. The answer is to define connectivity for neighboring pixels (voxels). To define connectivity, connected components (the application of graph theory to image processing and analysis) is a simple way of setting rules regarding which neighboring pixels or voxels are allowed to be connected together into separate objects. Figure 6 demonstrates connected components with a 2-D example. Figure 6a shows a pixel (2,2) with its surrounding neighbors. Pixel (2,2) has two types of neighbors: those that share an edge with (2,2) are shown in red and those sharing a corner are shown in green. The neighbors of pixel (2,2) can thus be defined solely as the red pixels in Figure 6a, solely as the green pixels, or as the union of these two sets. The definition used for neighboring pixels can strongly influence the number of objects as well as their shape and size, as demonstrated in Figure 6b with a small 5 × 5 pixel binary image with white pixels representing the ROI. If the neighboring pixels are defined solely as the red pixels in Figure 6a,

there are 5 unique objects (Figure 6c). If neighboring pixels are defined by the union of the red and green set in Figure 6a, there are only two unique objects (Figure 6d).

In 3-D, connectivity for voxels is very similar to that shown in Figure 6a, except there are three types of neighbors. Neighboring voxels can either be connected at cube faces, cube edges, or cube corners. Common connectivity rules for voxels are the six cube face neighbors, the six cube face neighbors plus the 12 cube edge neighbors, or all 26 surrounding neighbors. These configurations are shown in Figures 7a–c by the lines protruding from the representative cubic voxels.

The ability to connect neighboring voxels together is quite powerful. It allows the user to define unique objects and begin to assess each object individually within the imaged volume. Establishing connectivity is absolutely necessary for any statistically based analysis of material features as it defines the set of voxels belonging to each unique object.

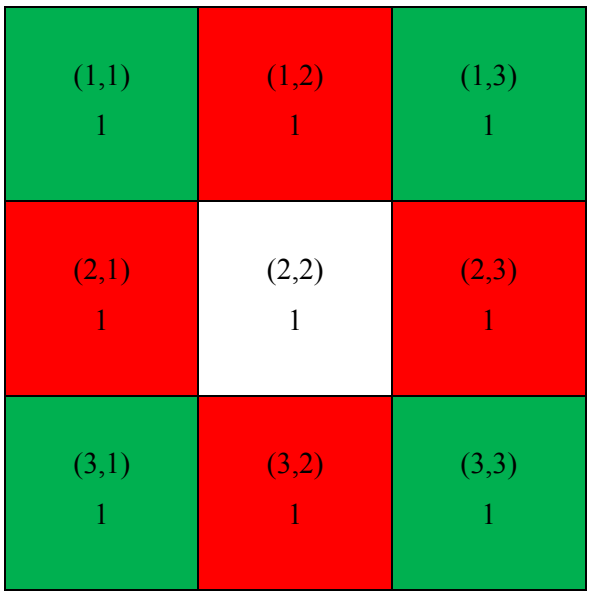

6a

(1,1) 0	(1,2) 1	(1,3) 1	(1,4) 1	(1,5) 0
(2,1) 1	(2,2) 0	(2,3) 0	(2,4) 1	(2,5) 0
(3,1) 0	(3,2) 1	(3,3) 1	(3,4) 0	(3,5) 1
(4,1) 1	(4,2) 1	(4,3) 1	(4,4) 0	(4,5) 0
(5,1) 0	(5,2) 1	(5,3) 0	(5,4) 0	(5,5) 1

6b

(1,1) 0	(1,2) 1	(1,3) 1	(1,4) 1	(1,5) 0
(2,1) 1	(2,2) 0	(2,3) 0	(2,4) 1	(2,5) 0
(3,1) 0	(3,2) 1	(3,3) 1	(3,4) 0	(3,5) 1
(4,1) 1	(4,2) 1	(4,3) 1	(4,4) 0	(4,5) 0
(5,1) 0	(5,2) 1	(5,3) 0	(5,4) 0	(5,5) 1

6c

(1,1) 0	(1,2) 1	(1,3) 1	(1,4) 1	(1,5) 0
(2,1) 1	(2,2) 0	(2,3) 0	(2,4) 1	(2,5) 0
(3,1) 0	(3,2) 1	(3,3) 1	(3,4) 0	(3,5) 1
(4,1) 1	(4,2) 1	(4,3) 1	(4,4) 0	(4,5) 0
(5,1) 0	(5,2) 1	(5,3) 0	(5,4) 0	(5,5) 1

6d

Figure 6. 2-D example of pixel connectivity.

Figure 6 visually demonstrates the application of 2-D connected components. Figure 6a illustrates the two types of neighboring pixels: face sharing (red) and corner sharing (green). Figure 6b is a synthetic image with labeled coordinates. Figure 6c illustrates the results of using just face-sharing neighbors to define connectivity within Figure 6b. Five objects result from this definition. Figure 6d is the result of defining all eight surrounding pixels as connected components. In this case, only two objects exist.

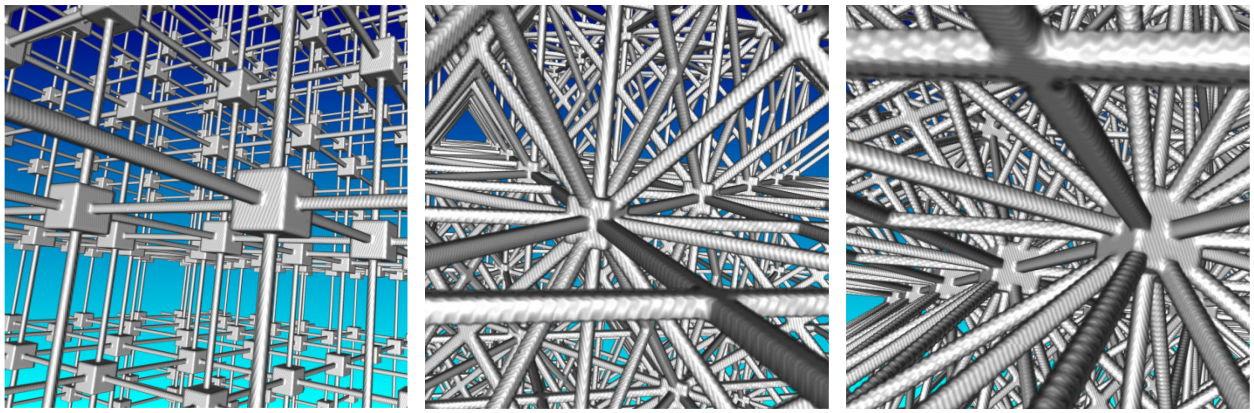

7a 7b 7c

Figure 7. 3-D visualization of voxel connectivity.

Figure 7 provides a visual representation of different connectivity rules in discrete 3-D space. Figure 7a represents six adjacent neighbors. The neighboring voxels are only connected on the six faces of a voxel. Figure 7b represents 18 adjacent neighbors. The neighboring voxels are connected along the six faces plus 12 voxel edges. Figure 7c represents all 26 adjacent neighbors. Neighboring voxels consist of the eight voxels touching at corners in addition to the 18 shown in Figure 7b.

2.3 Morphological Operations

Morphological operations are powerful image analysis techniques derived from mathematical morphology and are well-suited for the analysis of material structure. Morphological operators can be used to perform a wide variety of image processing and analysis functions including filtration, segmentation, image measurements, and a variety of other tasks such as minimal path detection. In this report only the two most basic operators (erosion and dilation) will be described as the other morphological operators can be obtained by the application of basic set theory to combinations of the erosion and dilation operators. For a more detailed coverage of morphological image analysis, the reader is referred to texts such as Pierre Soille's "Morphological Image Analysis."[15]

Prior to describing the basic morphological operators, three definitions should be given. The first is a structure element that describes a shape or sub-image used to investigate morphological properties of interest within an image. Figures 8a–f shows five structure elements within the $\boldsymbol{Z}^2$ domain. Structure elements 8c and 8d are commonly used in 2-D image processing, but structure elements can have arbitrary size and shape.

The second definition is the structure element reflection, denoted as $\hat{B}$, and can be defined as follows:

$$\hat{B} = \{w | w = -b, for\ b \in B\} \quad (1)$$

In other words, if B is a set of pixels within an image, then $\hat{B}$ represents a similar set of pixels where the coordinates change from (x, y) to $(-x, -y)$. In Figure 8, Figure 8B is the reflection of Figure 8A.

The final definition needed to describe the basic morphological operations is translation. Translation, denoted as $(B)_z$, can be defined as follows:

$$(B)_z = \{c | c = b + z, for\ b \in B\} \quad (2)$$

In the translation of B by $z = (z_1, z_2)$, if the coordinates (x, y) belong to B then the equivalent point in $(B)_z$ has the coordinates $(x + z_1, y + z_2)$, so $(B)_z$ shifts the image by (z_1,z_2).

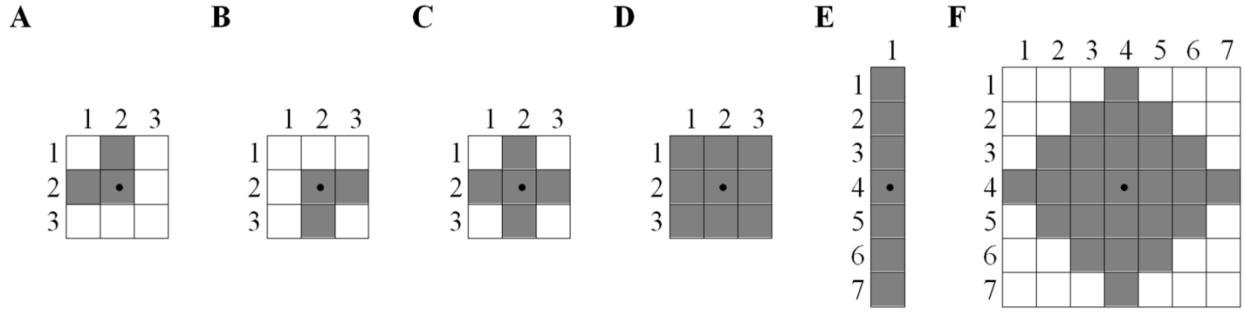

Figure 8. Structure elements.

Figures 8 a–f represent possible structure elements for use in morphological operations. The black circles represent the origin of the structure element. The origin does not have to be in the center of the structure element. Structure elements can have any size or shape, but are commonly significantly smaller than the image on which they operate. Figure 8c and 8d are commonly used structure elements in 2-D image processing.

2.3.1 Morphological Erosion and Dilation

Morphological erosion is defined as:

Erosion: $A \ominus B = \{z | (B)_z \subseteq A\}$ (3)

In words, erosion of A by B is the set of all points z for which the structure element B lies entirely within A. An example of erosion is shown in Figure 9b, where Figure 9a represents A, and B is the Figure 8C. Another way to think of erosion is replacing the value at the origin of the structure element by the minimum value observed within the kernel. Thinking of erosion in this way allows for proper execution of morphological erosion on a grayscale image. In Figure 8b, any location within the object where the structure element touches a white pixel (denoting zero) is replaced by zero and the original object is eroded away.

Complimentary to erosion is the dilation operator $A \oplus B$.

Dilation: $A \oplus B = \left\{ z \middle| \left(\hat{B}\right)_z \cap A = \emptyset \right\}$ (4)

Equation (4) states that the dilation of A by B is the set z for which at least one element of $\hat{B}$ lies within A (Figure 9c). The other way to think of dilation is replacing the value at the origin of the structure element with the maximum local value for that element. The dilation operation takes zeros along the edge of the object (Figure 9a) and replaces them with ones (Figure 9c) and the object appears to dilate relative to the original. Erosion and dilation can be useful by themselves for estimating the effects of uniform morphological change to objects, but they are also the building blocks for a majority of morphological operations. Several additional morphological operations are defined below with a brief description of their uses.

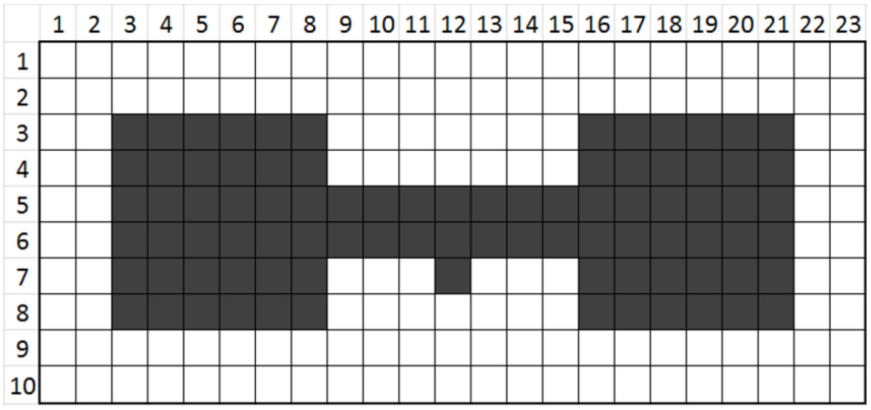

9a

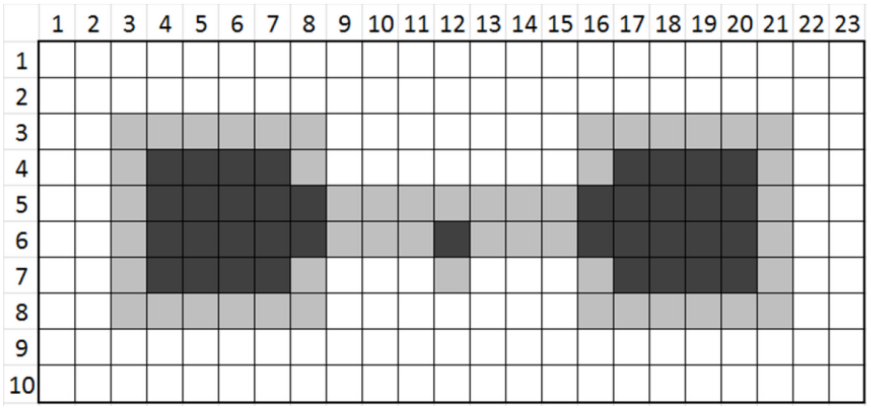

9b

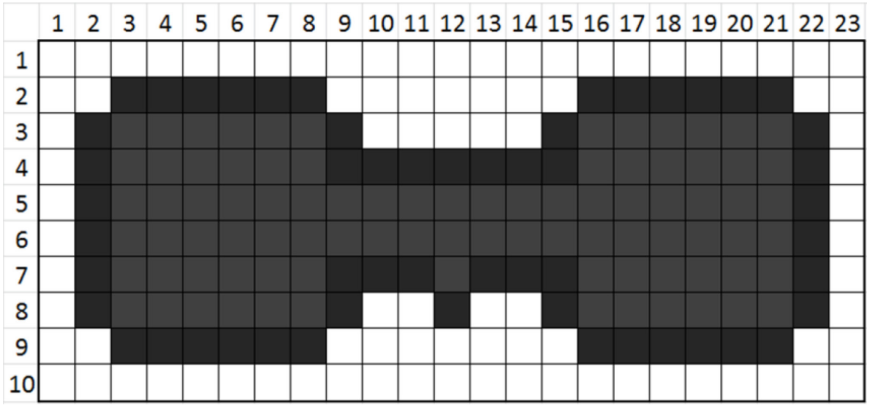

9c

Figure 9. Illustration of elementary morphological operators: erosion and dilation.

Figure 9 visually demonstrates the basic morphological operations of erosion and dilation. Figure 9a is the initial object image represent by A in Equations (3–9). Figure 9b is the result of binary morphological erosion of Figure 9a by the structure element in Figure 8c. The dark pixels represent the remaining pixels after erosion. The light pixels represent those that have been removed by erosion from A. Figure 9c is the result of binary morphological dilation of Figure 9a by the structure element in Figure 8c. The darker pixels represent those added via dilation. The lighter pixels are the subset of the resulting image that belonged to the original image, A.

2.3.2 Common Morphological Operations of Practical use in Materials Applications

Figure 10 can be used to demonstrate the morphological operations of opening, closing, and boundary extraction.

Opening: $A \circ B = (A \ominus B) \oplus B$ (5)

Opening will smooth surface contours, eliminate objects smaller than structure element B, and is capable of breaking small narrow interconnections between objects.

Closing: $A \cdot B = (A \oplus B) \ominus B$ (6)

Closing, like opening, can smooth contours, patch small holes (roughly the size of B), and connect objects spaced closely together.

As can be seen from Figures 10b and 10c opening and closing can remove objects or holes within the image without significantly affecting other features. Erosion and dilation alone would have removed the white circles and the small black circles, respectively, but in doing so would have significantly changed the size of all remaining features.

Boundary Extraction: $\beta(A) = A \cap (A \ominus B)^c$ (7)

Boundary extraction isolates the surface of objects within a data set. $(A \ominus B)^c$ represents the compliment of $A \ominus B$ (e.g., the boundary of Figure 10a is shown in Figure 10d).

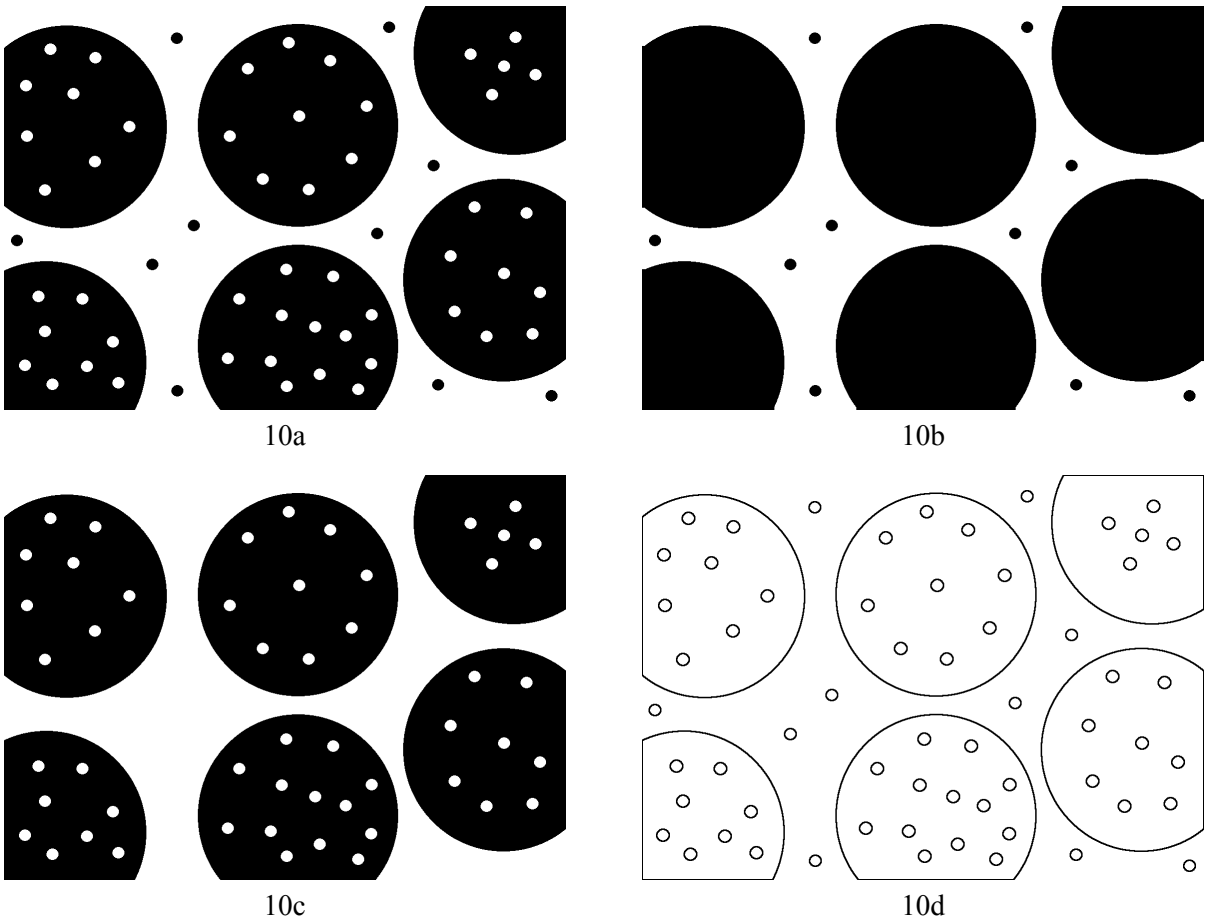

Figure 10. Illustration of morphological operators: opening, closing, and boundary extraction.

Figure 10 visually demonstrates morphological operations of opening, closing, and boundary extraction. Figure 10a is the original image and represents A in Equations (5–7). Figure 10b represents the morphological opening of Figure 10a. In Figure 10b and 10c, B is a circular kernel with dimensions approximately equal to the size of the small black and white circles in Figure 10a. Figure 10c represents the morphological closing of Figure 10a. Figure 10d represents the morphological extraction of pixels on the boundary of each object. B for Figure 10d is identical to Figure 8D.

Hit-or-Miss Transform: $A \circledast B = (A \ominus B_1) \cap (A^c \ominus B_2)$ (8)

The Hit-or-Miss transform is a basic tool for the detection of shapes. It is extremely useful when looking for very specific objects or features within an image. B_1 is the object/shape you are looking for in the image, and $B_2 = B_1^c$, where the c denotes the complimentary image.

Thinning: $A \otimes B = A \cap (A \circledast B)^c$ (9)

Thinning is useful for the reduction of objects, similar in many ways to pruning a tree or a bush. Pruning, which is a subset operator of thinning, can be used to remove parasitic branches from skeletons. An example of 3-D pruning is shown in Section 2.5, Figure 18.

Filling: $X_k = (X_{k-1} \oplus B) \cap A^c \quad k = 1, 2, 3, \ldots$ (10)

Finally, filling can be used to remove holes from objects. There may be some instances where artificial holes exist within objects due to the segmentation and these must be removed to properly analyze the object. In other cases, objects may inherently possess porosity or some other secondary phase that needs to be ignored in an analysis.

Equation (10) is an iterative process that continues until no additional changes can be made. In 2-D, A represents the original binary image and B is a symmetric structure element given by Figure 8C. The original array, X_0, is an array of zeros the same size as A. During the morphological operation, a single pixel/voxel with a value of 1 is placed in X_0 at coordinates corresponding to a pixel/voxel representing the hole to be filled.

2.4 Distance Transforms

Distance transforms are useful in image analysis as they provide a means for measuring distance within an image. There are two general types of distance transforms used in image processing and analysis, the Euclidean and geodesic distance transform. A good way to visualize the difference between these two transforms is the use of a simple maze. Distance between the maze entrance at p and the center at point q has two meaningful measures the Euclidean and geodesic distance. The Euclidean distance is easily defined as:

$$d_E = \|\vec{p} - \vec{q}\| \quad (11)$$

where $\vec{p}$ and $\vec{q}$ are the position vectors of points p and q on the maze and $\| \ \|$ represents the ℓ^2 norm. For the maze shown in Figure 11a, $d_E = 511$ pixel lengths.

The geodesic distance, on the other hand, represents the shortest distance someone would need to travel through the maze to go from p to q. Figures 11b and 11c show two possible paths through the maze. The path in Figure 11b is the shortest path with a length of 2,148 pixels; therefore it is the geodesic distance. The path in Figure 11c is feasible, but it is not the shortest path with a length of 3,055 pixels. By definition, this path is not the geodesic distance between points p and q. The geodesic distance transform is excellent for determining the shortest path through a ROI, but longer paths, such as the one in Figure 11c, are difficult to extract without a significantly larger computational investment.

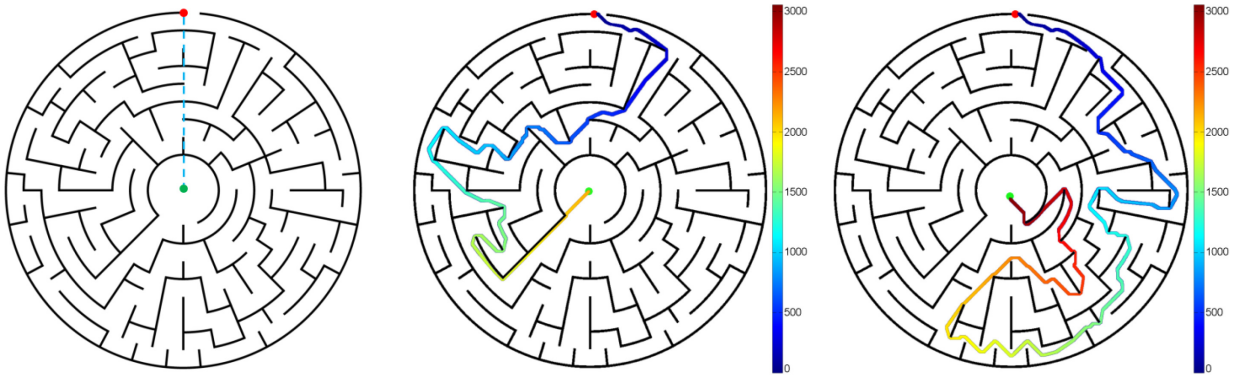

11a 11b 11c

Figure 11. Comparison of Euclidean and geodesic distances.

Figure 11 provides an illustration to compare Euclidean and geodesic distances. Figure 11a represents a "theta" maze with multiple distinct pathways from Point p to Point q. Points p and q labeled with red and green circles, represent the maze entrance and finishing point, respectively. In Figure 11a, the blue dashed line between Points p and q represent the Euclidean distance between p and q. Figure 11b represents the geodesic distance between p and q. Figure 11c is an alternative path through the maze between Points p and q with a significantly longer path length. The pathways displayed are based on a "chessboard" distance map (discussed in Section 2.4.1). The colormap superimposed onto the pathways is calculated from a "quasi-Euclidean" geodesic distance transform seeded at Point q.

Distance transforms are convenient for measuring distance between points from a Euclidean or geodesic perspective. For a Euclidean distance transform, distance is calculated from the interior of the ROI to the nearest pixel of the background. Figure 12a is the Euclidean distance transform of Figure 3b. In this case the Euclidean distance transform calculates how far each pixel of the INL logo is from the image background. For a geodesic distance transform (Figure 12b), the ROI is usually defined as the allowable set through which the transform can propagate. The user must also specify seed location, the origin point(s), for the resulting distance transform. The seed location will depend greatly upon the specific application and the feature to be measured. For the maze in Figure 11, the ROI is the interior white space of the maze and the seed point is the red dot (p) at the top of the image near the maze entrance (Figure 11).

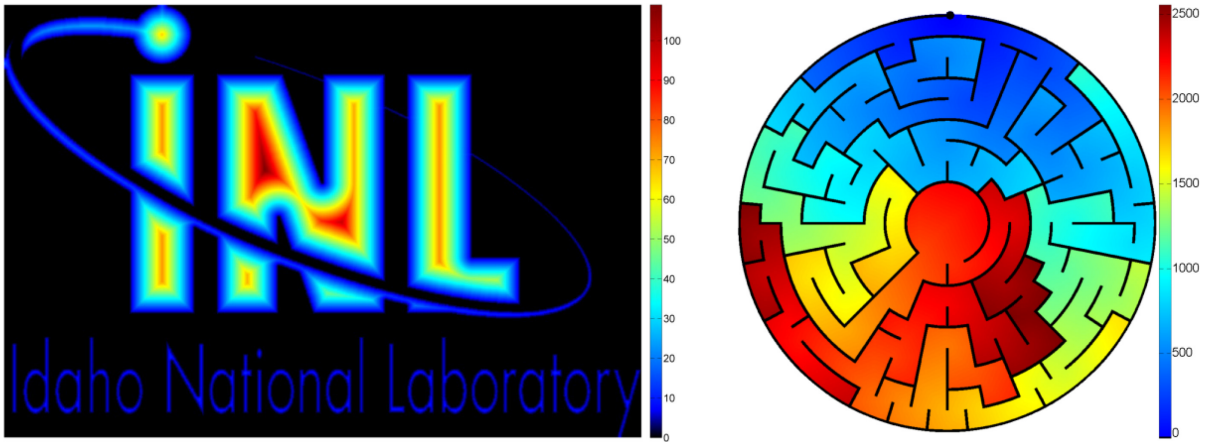

12a 12b

Figure 12. Distance transforms.

Figure 12 visually shows the results of Euclidean and geodesic distance transforms. Figure 12a representation of the Euclidean distance transform corresponding to Figure 3b. The color map represents the distance, in pixel lengths, from a black pixel to the nearest white pixel. Figure 12b is the resulting geodesic distance transform of Figure 11a with the seed location at point p.

2.4.1 Distance Metrics

A final consideration for the distance transform is how to determine distance. In discrete space, there are generally four standard metrics for distance. The metric used should consider computational expense as well as the accuracy with which the measurement must be made. This is especially important to consider for 3-D data sets as a significant amount of memory (tens to hundreds of GB) and computation time must be invested for large data sets. The first distance metric, often referred to as "city block" only advances to neighboring pixels (voxels) sharing a face. Referring back to Figure 6a, a distance transform seeded at (2,2) will advance to the red pixels in a first step and to green pixels in a second step. The distance traveled to reach the red pixels is 1 pixel length, while the distance traveled to reach the green pixels is two pixel lengths. The city block distance transform is illustrated in Figure 13a and Figure 14a for 2-D and 3-D, respectively. The city block distance transform is relatively inexpensive computationally, but is rather inaccurate along a diagonal.

Figures 13b and 14b visually demonstrate the results of the distance metric commonly referred to as "chessboard." As in the city block metric, the chessboard metric advances in units of one, but advances in a (1,1) equivalent direction in 2-D and (1,1,1) equivalent direction in 3-D space. The chessboard metric is significantly more accurate along the diagonal, while minimizing computational expense. The accuracy of the chessboard approach does suffer along a straight line.

"Quasi-Euclidean," the metric shown in Figure 13c and 14c, is a common method used for accurate determination of geodesic distances in constrained systems. Its distance front advances in units of one from pixel faces, and units of $\sqrt{2}$ from the pixel corners. As illustrated in Figure 14c, at relatively short distances its polyhedron nature is obvious; however, at longer distances (inset of Figure 14c) it appears nearly spherical. Figure 13d shows the Euclidean distance metric calculated as defined in Equation (10). The Euclidean distance metric is significantly more expensive, computationally, relative to the other distance metrics.

Figure 13 gives a visual representation of the four common distance metrics used two propagate a distance transform. Figure 13a represents the distance metric "city block" propagated outward three points within the image. Figure 13b represents the distance metric "chessboard" propagated outward from three points within the image. Figure 13c the "quasi-Euclidean" distance metric. Figure 13d represents the Euclidean distance metric. The actual distance transforms are represented by a gray-scale images with white representing the largest distance and black representing a distance of 0. Contour lines are shown at distance increments of 50 pixel lengths for Figure 13a–d.

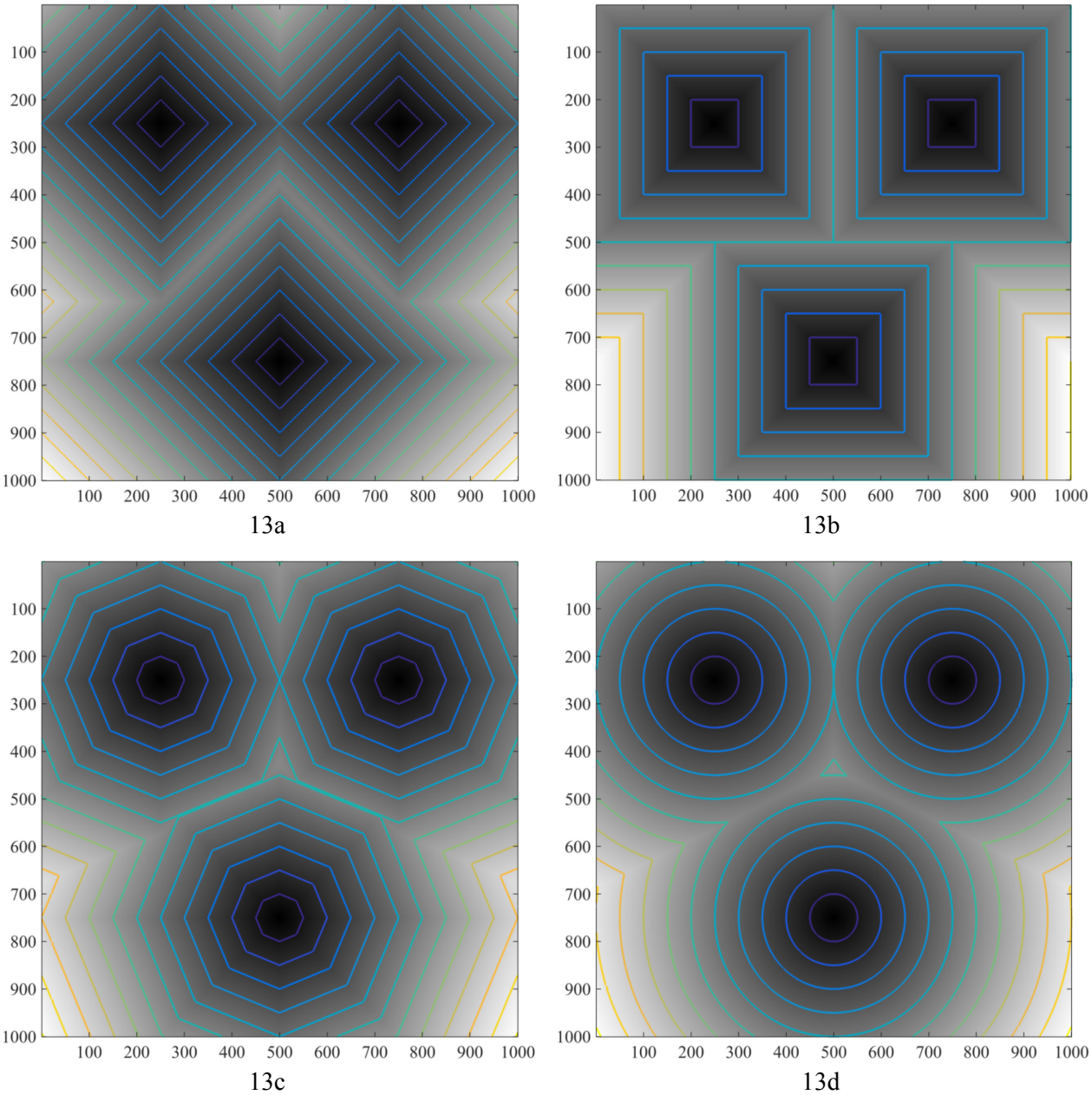

Figure 13. Distance metrics 2-D.

Figure 14 displays visual representations of the four common distance metrics used two propagate a distance transform. Figure 14a is an isosurface at a value of 150 for the distance metric “city block” propagated outward from the center of the image volume. Figure 14b is an isosurface at a value of 150 for the distance metric “chessboard” propagated outward from the center of the image volume. Figure 14c is an isosurface at a value of 50 for the “quasi-Euclidean” distance metric propagated outward from the center of the image volume. The inset in Figure 14c is the same propagated distance transform showing an isosurface at a value of 150. Figure 14d is an isosurface at a value of 150 resulting from a Euclidean distance metric used for propagation of the distance transform.

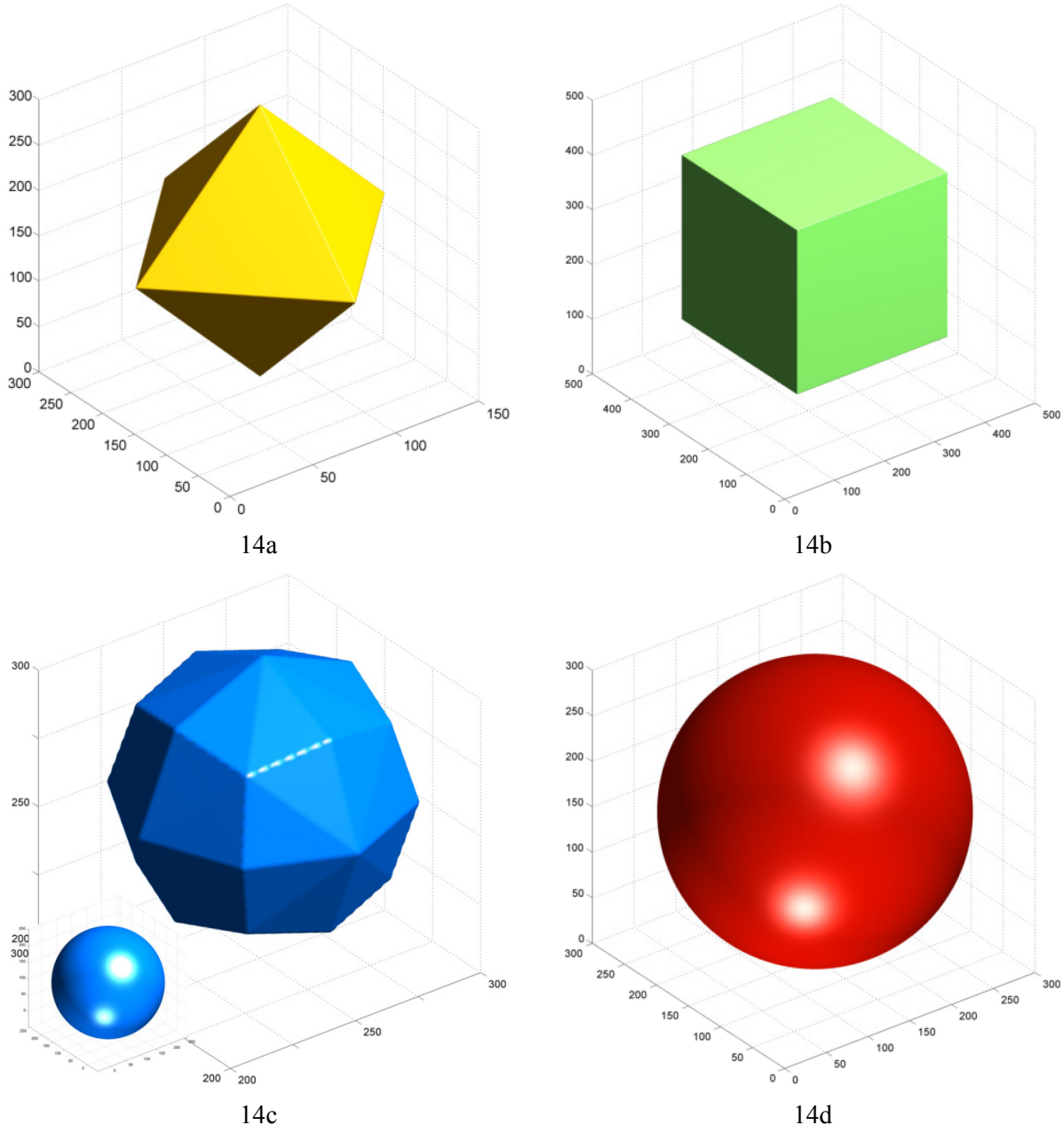

Figure 14. Distance metrics 3-D.

2.4.2 Watershed Segmentation

As a brief aside, there are some cases where typical segmentation works very well, but does not actually separate individual objects touching 3-D space. A visual example is shown in Figure 15a, which is a 3-D data set imaging 299 mullite milling media bead suspended in an epoxy resin. The major obstacle to image analysis for cases such as this is the fact that many objects are touching one or more others, making the analysis in this case of the individual beads impossible without further processing. A technique called watershed segmentation can be used to separate touching objects to allow further analysis. This technique is discussed here rather than in Section 2.1 because watershed segmentation relies on the use of a Euclidean distance transform as the initial input. Figure 15b shows the milling media separated into different objects allowing individual beads to undergo additional image processing and analysis separately (Figure 15c and 15d).

Watershed segmentation in many ways is analogous to its namesake. A watershed is a region or area bounded peripherally by a divide and draining ultimately to a particular watercourse or body of water. In other words, all water that falls within a particular watershed will ultimately flow to the same location. Using a Euclidean distance transform, an artificial elevation map can be created to help separate touching objects.

Figure 16 visually illustrates the general process of watershed segmentation. Figure 16a shows 12 overlapping ellipses. A Euclidean distance transform is used to determine the distance from each white pixel within the object to the nearest black pixel (Figure 16b). Figure 16c is essentially a 3-D surface representation of Figure 16b, but shows that the distance transform can be used as an artificial elevation map where the distance away from the object edge represents a depth. The actual details behind watershed segmentation are beyond the scope of this report, but it is sufficient to say that the watershed algorithm can determine boundaries between different watersheds. The watershed boundaries are often a good representation of borders between overlapping objects in 2-D (Figure 16d) and touching objects in 3-D.

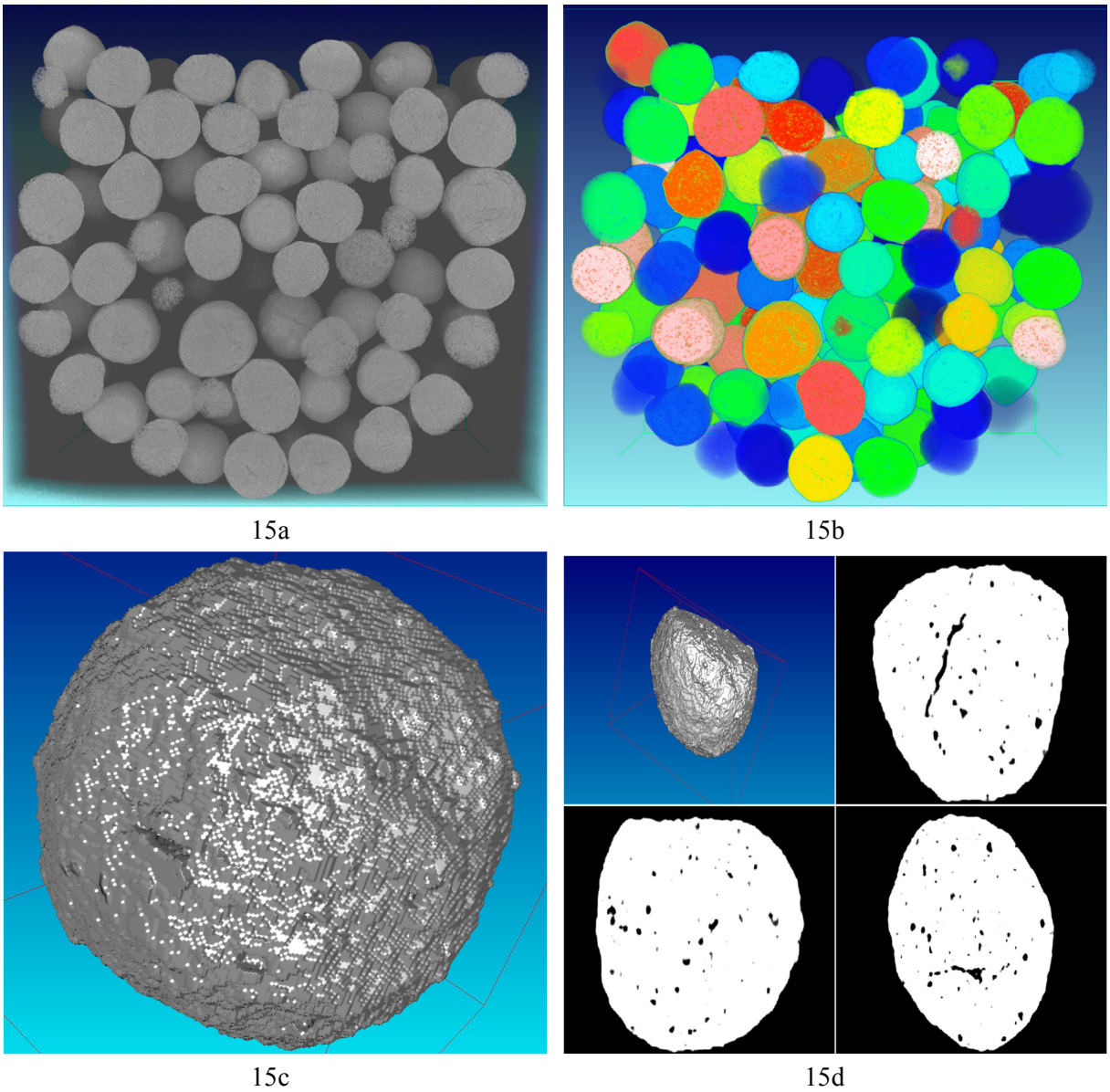

15a 15b

15c 15d

Figure 15. Segmentation of milling media using watershed segmentation.

Figure 15 demonstrates the application of watershed segmentation to identify individual milling media beads within the scanned 3-D volume. Figure 15a is a reconstructed 3-D projection of 299 mullite milling media beads. Figure 15b is the same 3-D projection, after watershed segmentation has been applied to separate individual particles. A false color map is applied to highlight that beads are no longer connected. Figure 16c shows a 3-D projection of a randomly selected bead from the compact. Figure 16d shows a similar randomly selected bead with 3 slices shown. The slices show the inherent porosity of the beads which could be further analyzed with respect to each bead. The slices are orthogonal to the x, y, and z axis.

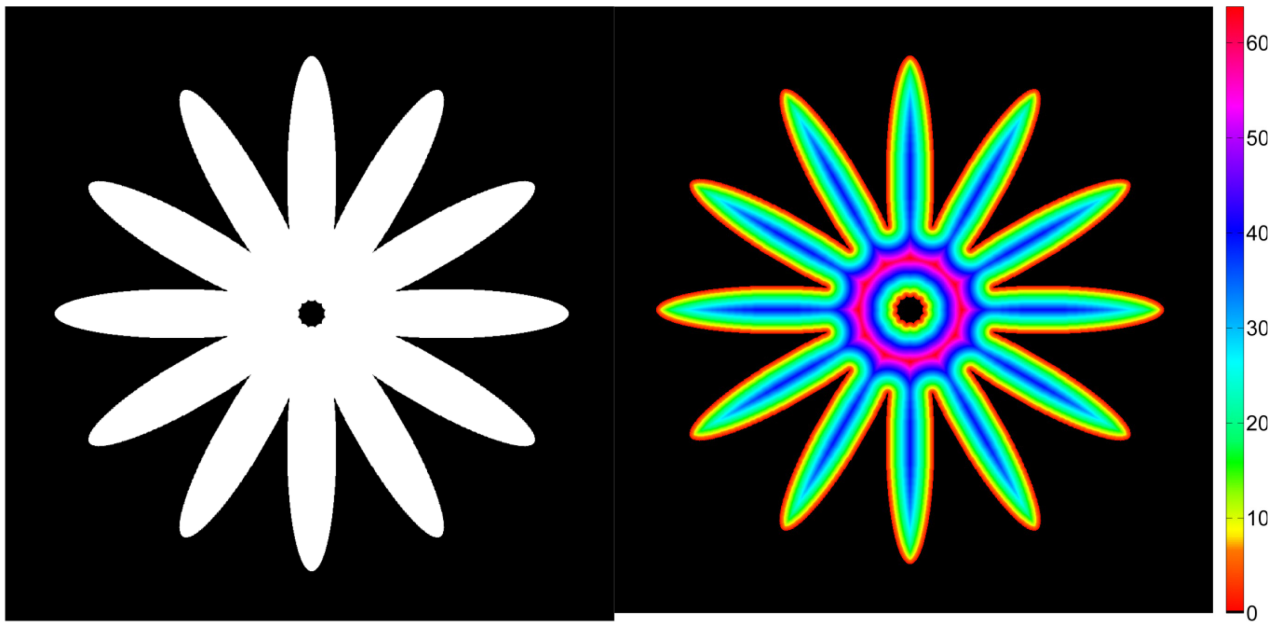

16a 16b

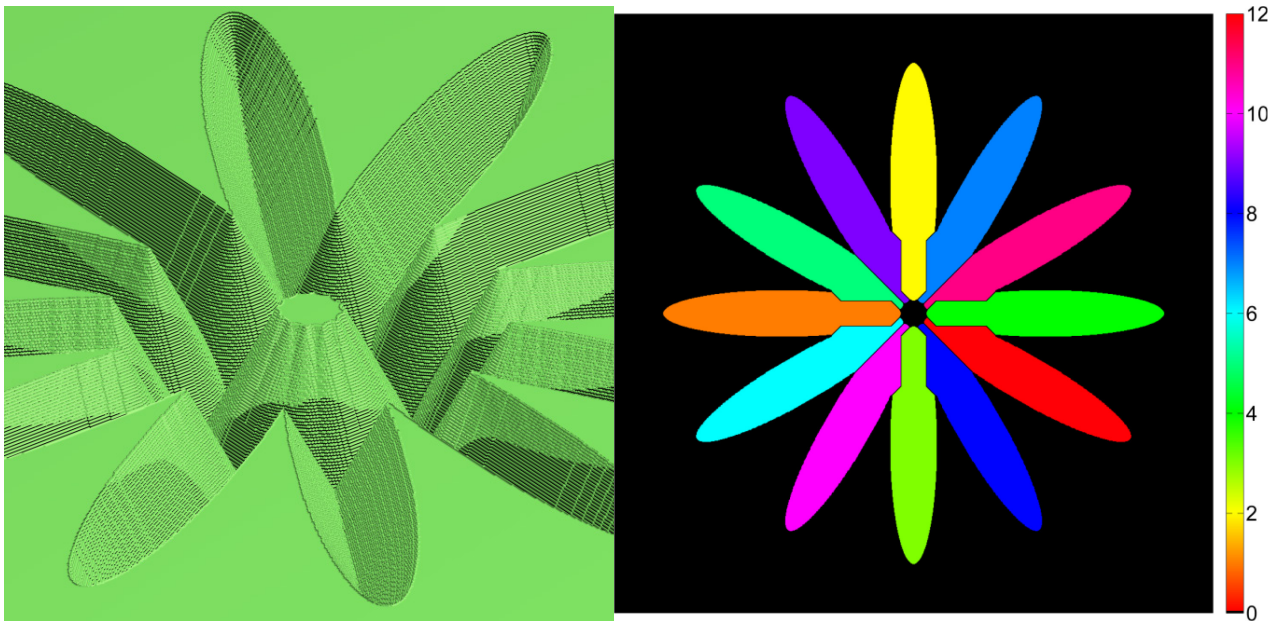

16c 16d

Figure 16. Watershed segmentation 2-D illustration.

This figure demonstrates a basic watershed segmentation algorithm. Figure 16a is a synthetic image of 12 ellipses superimposed upon each other and offset by 30-degree rotations about the center of the image. Figure 16b is the corresponding Euclidean distance transform of Figure 16a. The color map represents the distance measured in pixel lengths from each white pixel in Figure 16a to the nearest black background pixel. Figure 16c is a topographical representation of the Euclidean distance map in Figure 16b. Figure 16d is a colored image representing each indexed object after applying a watershed segmentation algorithm. The color map defines the color of the indexed object.

2.5 Skeletonization

The final subject discussed in this section is skeletonization. Skeletonization is the reduction of an object to its essential framework, in some sense it is a center-lined minimalistic "sketch" of the object. Skeletonization is a useful tool in image analysis because it provides a compact object representation, yet still conserves much of the object's character (size and shape) and connectivity. A human silhouette and its skeleton, or medial axis, is shown in Figures 17a and 17b.

Skeletonization is used extensively in pattern recognition and shape analysis to extract information on the object's shape. Quite often the skeleton is used to detect branch points, end points and closed loops, which are in turn used for object classification into a shape category. In Figure 17c, the end points of the skeleton and nearest branch points were used to identify and label appendages of the original silhouette. Skeletonization has obvious utility in materials science for materials with network-like structures, such as interconnected porosity where the number and locations of closed loops and branch points may be of quantitative interest.

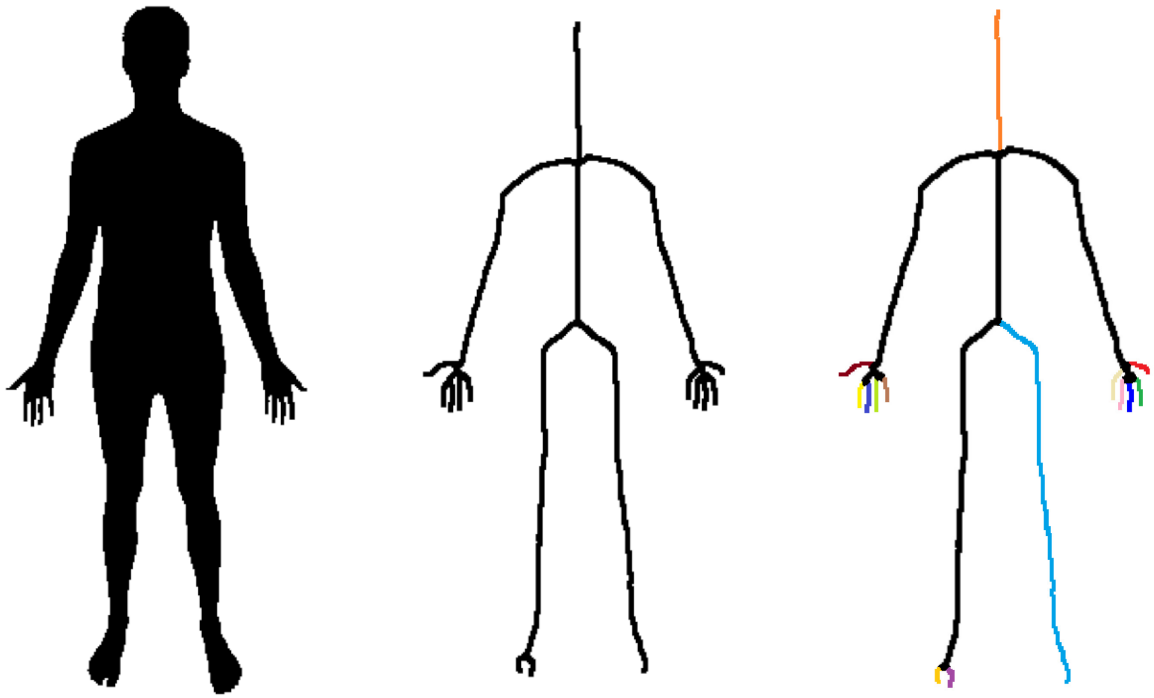

17a 17b 17c

Figure 17. Skeletonization.

Figure 17 represents skeletonization and possible extracted information. Figure 17a is a binary image showing the silhouette of a human male. Figure 17b is the skeleton of Figure 17a. The skeleton is dilated to enhance visibility. Figure 17c shows highlighted branches of the skeleton in Figure 17b indicating limbs or appendages.

Skeltonization in both 2-D and 3-D is often quite sensitive to slight changes in curvature that may exist due to "noise" at the object/background interface at segmentation. While many algorithms take measures to reduce this sensitivity, inevitably unwanted (and erroneous) artifacts known as parasitic branches are produced during skeletonization. Morphological smoothing pre-filters can be used to reduce the amount of parasites, but ultimately morphological pruning is needed to remove the remaining erroneous branches. Figure 18a and 18b show the skeleton of a SiC foam structure pre- and post-pruning. The results of pruning here are visually quite apparent.

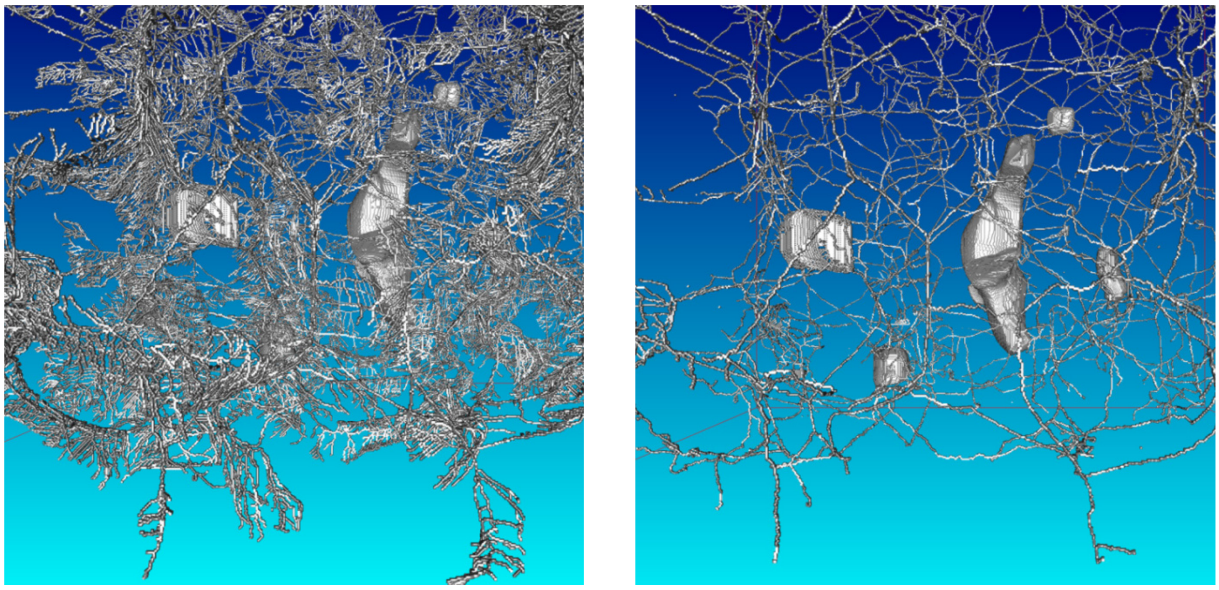

18a 18b

Figure 18. Silicon carbide foam skeleton.

Figures 18a and 18b shows the skeleton of a SiC foam structure before and after morphological pruning. The large objects within Figures 18a and 18b are hollow regions within the SiC foam.

2.6 Summary of Principles and Concepts for 3-D Image Analysis

The principles and concepts discussed previously are some of the primary building blocks for image analysis. Image segmentation (Section 2.1) and connected components (Section 2.2) are paramount as they must be successfully implemented prior to almost any conceivable analysis. Image segmentation in many respects is the critical step in image analysis once the fundamentals of image processing and analysis are understood since getting a computer to duplicate what the human eye segments automatically can at times be technically very difficult.

It is also the opinion of the authors that morphological operators, distance transforms, and skeletonization techniques are particularly useful in quantitatively examining 3-D material volumes. With few exceptions, nearly all physical measurements can be performed using these three tools individually, or in a plethora of unique combinations.

Section 3 is dedicated to real application of these tools to characterize a variety of materials of interest to the nuclear materials community. The examples in Section 3 implement a number of principles and concepts from Section 2 illustrating the increased information available from 3-D analysis of the volumetric data. The first example material utilizes Image Segmentation and Connected Component principles. The second example material utilizes distance transforms in addition to image segmentation and connected components. Finally, the third material example incorporates all techniques introduced in Section 2 to illustrate the complexity that can be achieved with a 3-D analysis.

3. NUCLEAR MATERIALS APPLICATIONS

3.1 Overview

In Section 2, several principles and concepts were briefly covered to provide basic understanding of some of the common tools used for segmentation and ultimately the extraction of quantitative information from a 3-D volume representing a material. Section 3 focuses on the application of these fundamental principles and concepts to INL's relevant nuclear materials. This section is meant to give the reader practical examples of quantitative image analysis.

Three nuclear materials from three INL programs have been chosen as example materials to provide practical demonstrations of 3-D image analysis. Each material system was selected in order to illustrate different capabilities and the quantitative data available from a 3-D image analysis. To illustrate the progressive application of the various analysis techniques the complexity of the analysis is increased with each subsequent material example

The initial example uses relatively simple image segmentation and connived components techniques applied to preliminary surrogate TREAT fuel compacts to discern particle size distribution and crack formation from processing. Additional analysis techniques (segmentation, connected components, morphological, and distance transforms) are required to investigate fuel compacts containing TRISO fuel particles being developed for the ART AGR program. Finally, the complex microstructure and detailed analysis of nuclear graphite requires the full complement of analysis techniques including skeletonization to map out the complex defect pore structures in a graphite sample. A brief introduction is provided for each example material system outlining the importance the importance of the material and the value of the analysis. This is followed by a short description of the analysis itself and an outline of the basic processing steps needed to complete the analysis.

It should be noted that the practical material examples discussed in this report are quite significant in size; therefore, significant computing resources are needed. For this report, INL researchers made use of the High Performance Computing Center at INL, which is supported by the Office of Nuclear Energy of the U.S. Department of Energy (DOE). Funding for analysis of TREAT fuel compacts was provided by the National Nuclear Security Administration's (NNSA) Office of Material Management and Minimization Reactor Conversion Program. Funding for AGR compact, AGR TRISO particles, and nuclear graphite was provided by the Advanced Reactor Technology (ART) program.

3.2 Preliminary Transient Reactor Test Facility Low Enriched Uranium Conversion Fuel Compact

The development of new accident-tolerant nuclear fuels, new fuel designs, and proliferation resistant nuclear fuel forms has created an increased need to test these fuels under nuclear accident conditions. The DOE is updating the USA's capability to conduct transient testing of nuclear fuels. During transient testing, nuclear fuel and materials are subjected to short bursts of intense, high-power radiation inside the cores of specifically designed test reactors. The fuel and material is then analyzed to determine the effects resulting from various levels of exposure.

The TREAT reactor at INL is being re-established and updated to support this needed capability. TREAT was designed and built specifically to support transient testing of nuclear fuels and materials. It is capable of "stress testing" nuclear fuels with quick, high-energy neutron pulses that mimic accident conditions. Previously it has been used to design durable nuclear fuels, establish performance limits, validate design codes, and assist in defining safety limits for new nuclear reactor core designs.

TREAT has not been operated for over 20 years and the original core was designed and built before 1959. After such a long period since operation, significant modifications to the entire facility are necessary to resume transient testing. One of the most significant modifications anticipated is conversion

of TREAT fuel to low-enriched uranium (LEU). The fuel will essentially consist of a diluted mixture of fine low-enriched UO_2 particles in a carbonaceous/graphitic matrix. During transient operation, the core design must permit rapid transfer of fission energy into the graphite and carbon, resulting in a rapid and uniform heat up of the moderator (carbon and graphite). The uniform heating of the moderator material results in a nearly instantaneous, negative-temperature coefficient of reactivity, and hence, self-limiting nuclear transients.

X-ray CT and image analysis have been employed at INL to non-destructively assess the microstructure of preliminary batches of surrogate compacts. The main features of interest were the fine ZrO_2 particles used as a fuel surrogate for UO_2 and identification of crack formation during the compaction and subsequent heat treatment (Figure 19a and 19b). A particle size analysis was used to assess agglomeration of the surrogate particles during compact production and a Hotelling transform (known in other fields as a principal components analysis) was used to assess the size, shape, and orientation of cracks produced during the fabrication process. For more detailed information, refer to the 2016 article published in Nuclear Engineering and Design by Kane et al.[18]

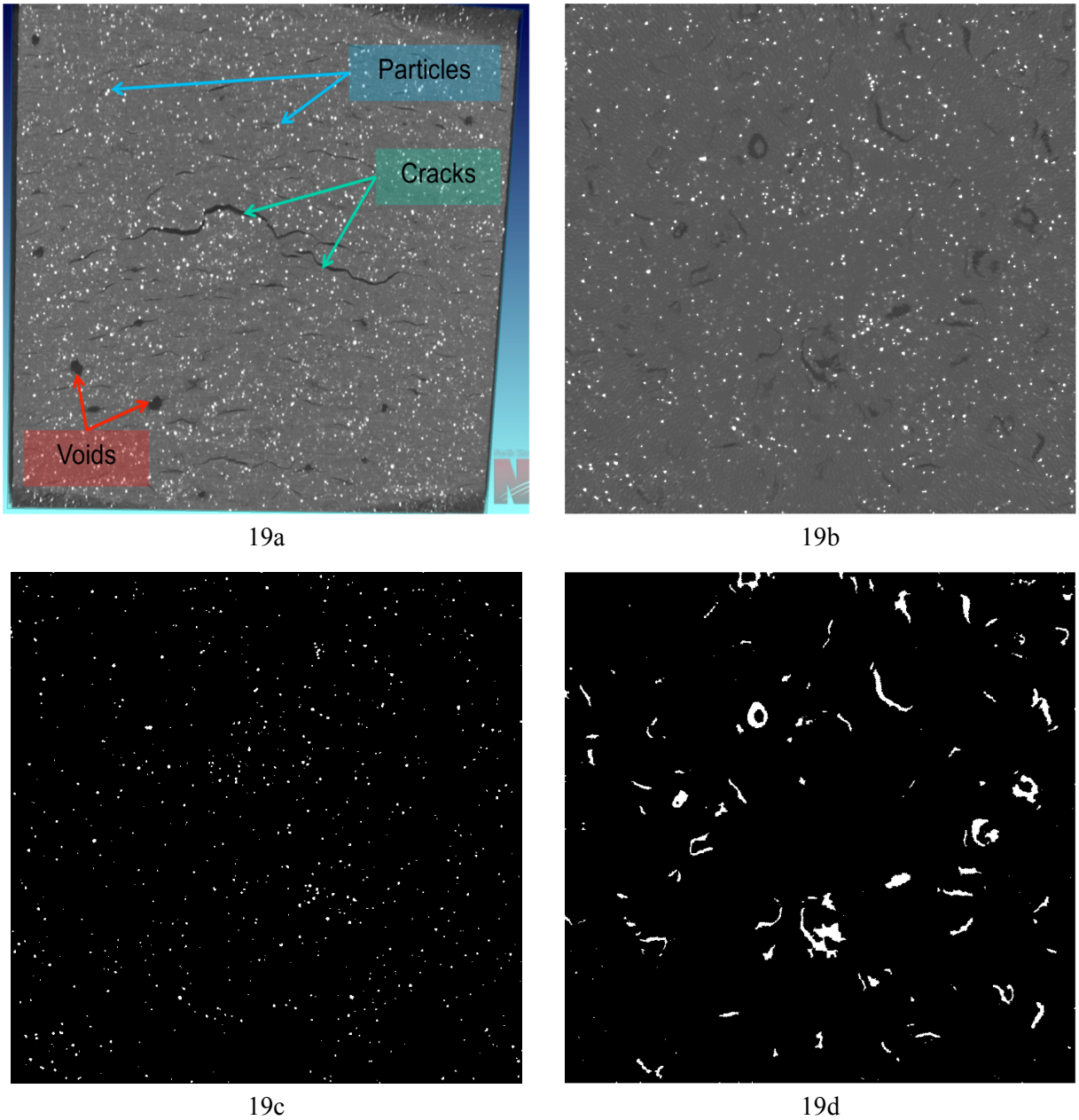

19a 19b

19c 19d

Figure 19. Treat fuel compact microstructure.

Figure 19 shows the structure of a scanned preliminary TREAT fuel compact and the segmented surrogate fuel kernels and voids. Figure 19a is a 3-D image of 3-D slices from the x, y, and z planes that intersect the center of the 3-D volume. Figure 19b is the 2-D image of the z plane shown in Figure 19a. Figures 19c and 19d are the resulting selective segmentations of the surrogate fuel kernels and voids, respectively.

3.2.1 Particle Size Distribution

Prior to fabrication, a substantial amount of modeling and simulations efforts were undertaken to determine a maximum allowable particle size for the LEU UO_2 fuel. The maximum particle size for the fuel design was set at 44 μm, equivalent to the approximate opening of a 325-mesh sieve. A uniform spatial distribution of particles with a diameter less than this specified engineering limit, will allow the

fuel blocks to achieve the desired performance levels while still providing a significant margin of error for removal of heat from the individual particles. As a particle's size increases, the expected maximum temperature of the particle will increase substantially. By providing engineering limits on the maximum particle size, several life-limiting concerns, including melting of the particles during operation, are avoided.

While the ZrO_2 surrogate powder was sieved to exclude particles with a diameter greater than 44 μm, agglomeration could result during manufacturing leading to effect diameters greater than the maximum specified in the design. A particle size distribution was used to assess the degree of agglomeration that occurred under a variety of fabrication conditions. A representative particle size distribution is shown in Figure 20a and a comparison of mean values for various batches is shown in Figure 20b. A particle size distribution was obtained from the data volume using the following methodology:

1. An automated global threshold routine was used to segment the ZrO_2 particles (Section 2.1.1).
2. A connected components algorithm was used to identify individual particles (Section 2.2). The connectivity used was equivalent to Figure 6c.
3. The number of voxels belonging to each object was determined from the unique index of each object.
   a. This was converted to a volume using calibrated voxel dimensions
4. An effective particle diameter was determined by assuming each object was spherical.

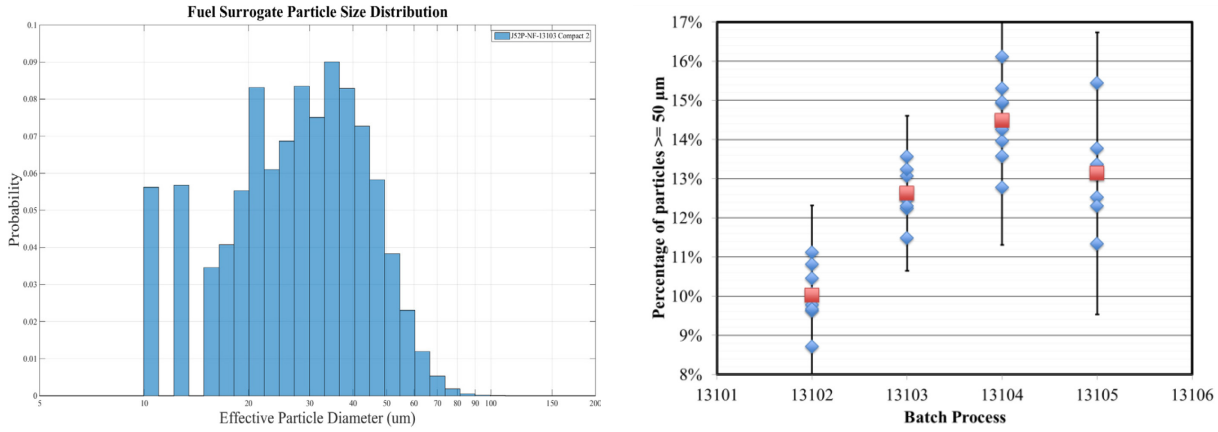

20a 20b

Figure 20. Analysis particle size distribution in preliminary TREAT LEU fuel fabrication process.

Figure 20a show a typical particle size distribution resulting from the examination of TREAT preliminary surrogate fuel compacts. Figure 20b shows slight variations in the amount of agglomeration observed in each preliminary batch.

From the information collected from 32 preliminary compacts from four different batches with varying processing parameters, an estimate of the amount of agglomeration was determined. Based on this information, a wetting agent was used in subsequent production to reduce the degree of agglomeration.

3.2.2 Size, Shape, and Orientation Analysis of Cracks

As shown in Figure 21a and 21b, cracks produced during the compaction and subsequent heat treatment are rather aspherical and appear to have a preferred orientation within the structure. The size, shape, and orientation of these cracks were of interest as they are considered detrimental to the mechanical properties of the compact. Depending on their origin, the cracks could increase in size as the fabrication process was scaled up.

The shape of the cracks observed in these compacts was ideally suited for analysis via a Hotelling transform. The Hotelling transform essentially fits an ellipsoid to each object from which information regarding its length, shape, and orientation can be extracted. The Hotelling transform was essentially implemented as follows:

1. An automated global threshold was routine and was used to segment cracks from the surrounding matrix material (Section 2.1.1).
    a. Prior to segmentation, filtering was necessary to maximize accuracy of segmentation.
    b. Post segmentation, morphological filling (Section 2.3.2) was used to remove small non-physical holes within the segmented cracks.
2. A connected components algorithm was used to identify individual particles and extract the coordinates of each voxel belonging to a specific crack (Section 2.2).
3. Coordinates were translated so the crack center of mass was at the origin
4. The covariance matrix, a 3 × 3 matrix, was formed from the translated coordinates of a cracks voxels.
    a. Refer to any linear algebra textbook for details.
5. Eigen values and Eigen vectors of the covariance matrix were determined
    a. Eigen values are directly proportional to the length of the three principle axes of the corresponding ellipsoid that best fits the crack
    b. The Eigen vectors correspond to the orientation of the three principle axes of the best fitting ellipsoid.

Figure 21a and 21b show 3-D projections of the 100 largest cracks within a TREAT preliminary fuel compact. Figure 21c is a histogram showing the probability of having a crack of a given size. Figure 21d shows the orientation distribution of the primary, secondary, and tertiary axes of the ellipsoid that best fits the crack.

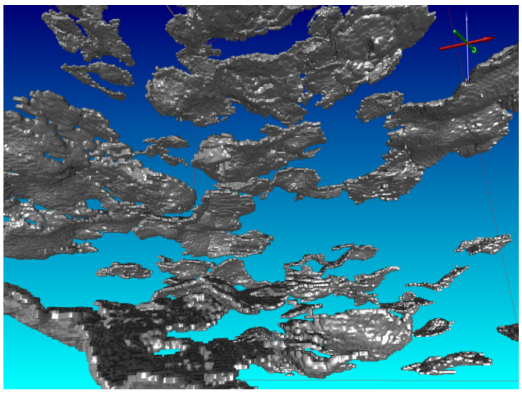

21a

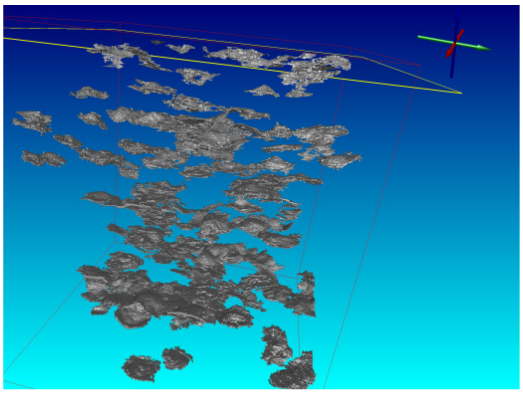

21b

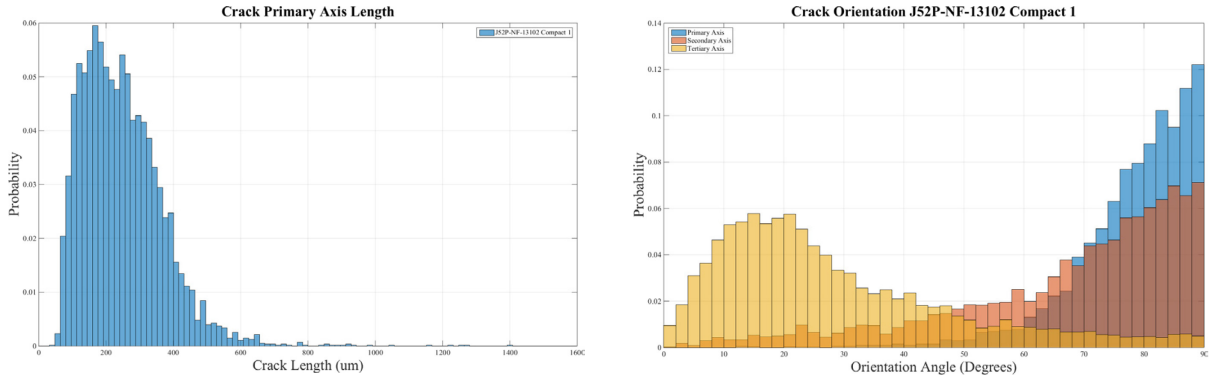

21c 21d

Figure 21. Shape and orientation analysis.

3.3 Advanced Gas Reactor Fuel Compacts and Tristructural Isotopic Particles

The Advanced Reactor Technologies (ART) AGR fuels program is the largest research activity within the high-temperature reactor (HTR) program. The HTR concept is a helium-cooled, graphite moderated, thermal neutron spectrum reactor with a design goal outlet temperature of 750°C to 1000°C (i.e., the very high temperature design). The graphite-based core can be either a prismatic graphite block type core or a pebble bed core design. The HTR is designed to produce both electricity and process heat for chemical processes such as hydrogen generation. The reactor thermal power and core configuration is designed to assure passive decay heat removal without fuel damage during hypothetical accidents. The fuel cycle is a once-through very high burnup LEU fuel cycle.

The fuel for the HTR builds upon the potential of the TRISO coated particle fuel design. The TRISO coated particle is a spherical layered composite about 1 mm in diameter. It consists of a kernel of uranium oxycarbide (UCO) surrounded by a porous graphite buffer layer that absorbs radiation damage, allows space for fission gases produced during irradiation, and resists kernel migration at high temperature. Three additional layers surround the buffer layer: a layer of dense pyrolytic carbon, a SiC layer, and a dense outer pyrolytic carbon layer, Figure 22c and 22d. The pyrolytic carbon layers shrink under irradiation and provide compressive forces that act to protect the SiC layer, which is the primary pressure boundary for the TRISO micro-sphere. The inner pyrolytic carbon layer also protects the kernel from corrosive gases that are present during the deposition of the SiC layer. The SiC layer acts as a primary containment vessel for fission products generated during irradiation and under accident conditions. Each TRISO micro-sphere acts as a mini pressure vessel—a feature that is intended to impart robustness to the gas reactor fuel system.

For the pebble bed version of an HTR, the coated particles are over-coated with a graphitic powder and binders. These over-coated particles are then mixed with additional graphitic powder and binders and molded into a 5-cm sphere. An additional 0.5-cm fuel-free zone is added to the sphere prior to isostatic pressing, machining, carbonization, and heat-treating.

For the prismatic version of the HTR, a similar process is used where the over coated particles are mixed with graphitic powder and binders to form a cylindrical compact approximately 5 cm long and 1.25 cm in diameter. After final heat treatment, these compacts are inserted into specified holes in the graphite fuel blocks Figure 22a and 22b.

Understanding the effects of processing and fabrication on microstructure is vitally important to successfully qualifying fuel for an HTR. Additionally, the fuel for both the prismatic and pebble bed design will undergo significant microstructural change under the extreme temperature and neutron

irradiation conditions of the HTR. To successfully license HTR technology and take full advantage of the very high burnup fuel cycle for 40+ years, microstructural changes will need to be quantified using modelling efforts.

Three-dimensional image processing and quantitative analysis is capable of probing the microstructure of the fuel and individual TRISO particles to quantify the initial microstructures as well as changes in microstructure after irradiation in a reactor environment. Section 3.3.1 and Section 3.3.2 will discuss a few of the many possible ways to quantitatively characterize fuel and individual TRISO particles, respectively. In the following sections the fuel compacts have Al_2O_3 particles as surrogates for the TRISO fuel and the TRISO particle example contains an Al_2O_3 kernel. The characterizations discussed can provide valuable and previously inaccessible information for the ART AGR fuels program as demonstrated by other material researchers using 3-D characterization techniques.[19]

Figure 22a shows a gray-scale slice across an AGR compact. Figure 22b is a 3-D projection of the surrogate particles and cracks within the volume of the compact. Figure 22c is a slice of a single TRISO particle with a fuel surrogate composed of Al_2O_3. Figure 22d is a 3-D projection of the TRISO particle shown in Figure 22c.

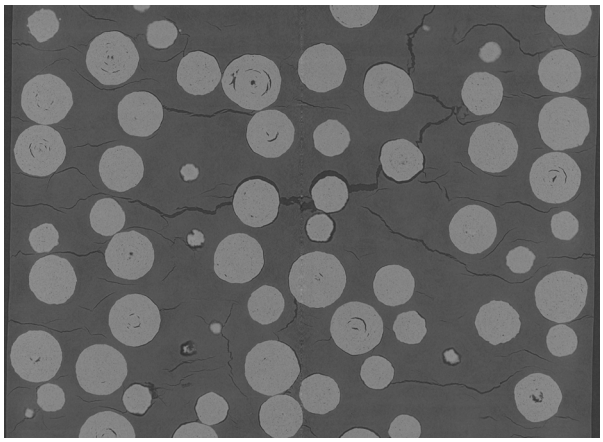

22a

22b

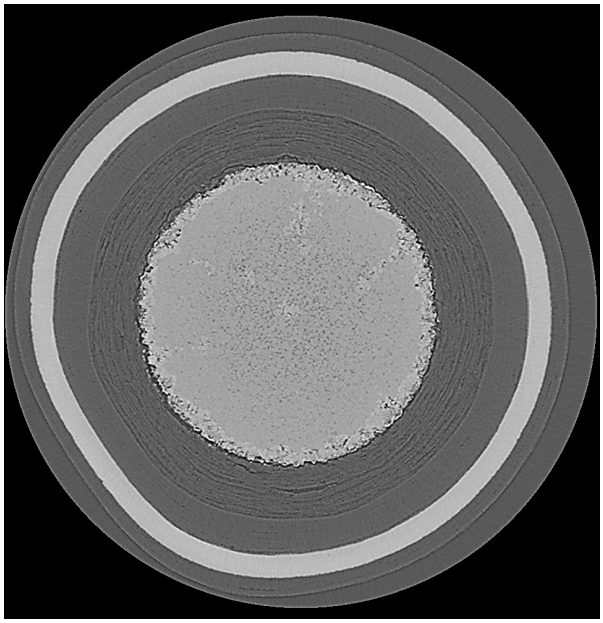

22c

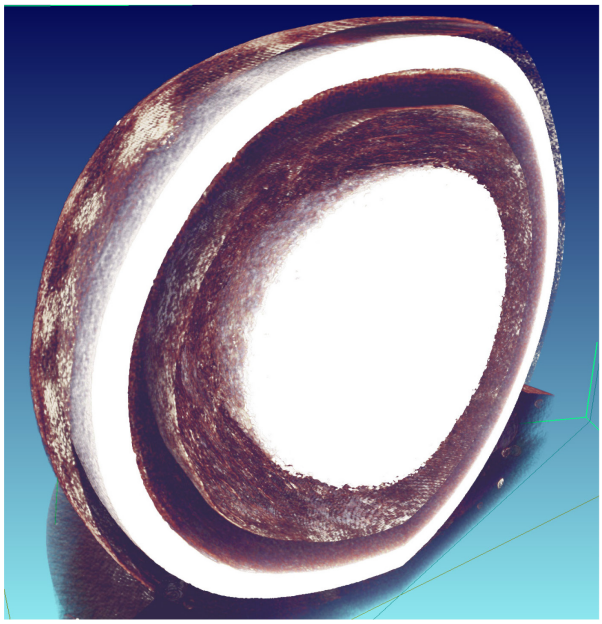

22d

Figure 22. AGR surrogate fuel compact and AGR surrogate TRISO particle.

3.3.1 AGR Surrogate Fuel Compacts

The 3-D analysis of AGR compacts has the potential to provide a significant amount of microstructural information to researchers in the ART fuels program, specifically, information regarding the particle size distribution, crack size shape, and orientation, and information regarding the local packing fraction distribution within the compact. As shown for the preliminary TREAT compacts (Section 3.2.1), particle size distributions can be determined free of the assumptions needed when attempting to make similar measurements from cross-sections. The cracks within the matrix, similar to TREAT can also be characterized. Since these types of analyses have already been discussed in Section 3.2, this section will focus on determining spatial distributions of surrogate particles within the AGR compact.

Determining a property over a local region can be accomplished with relatively ease using a discrete 3-D correlation. The 3-D discrete correlation takes the mathematical form

$$w(x,y,z) \star f(x,y,z) = \sum_{s=-a}^{a} \sum_{t=-b}^{b} \sum_{u=-c}^{c} w(s,t,u) f(x+s, y+t, z+u) \quad (12)$$

where w represents a 3-D kernel or filter and f represents the data volume to be analyzed. Additionally,

$$a = (m-1)/2 \quad (12a)$$

$$b = (n-1)/2 \quad (12b)$$

$$c = (p-1)/2 \quad (12c)$$

and m, n, and p represent the dimension of w. For notational and computational convenience, m, n, and p are assumed to be odd integers. If f represents a binary 3-D volume (in this specific case a binary volume of surrogate particles) allowing w to equal a 3-D matrix of ones, the discrete correlation effectively counts the number of voxels equal to 1 within f over a region specified by w. With minor manipulation this can be interpreted as a local packing fraction. For this specific correlation, w is symmetric, and thus the correlation is identical to a discrete convolution. Many numerical computation software programs such as MATLAB® contain discrete convolution functions within their built-in libraries.

1. Determine a reasonable kernel size for w, the average particle size distribution was determined (Section 3.2.1)
    a. The dimensions of w were set to that of a face-centered cubic structure with close packed spheres equal in diameter to the maximum particle diameter within the compact.
2. Masked the volume over which the analysis was pertinent and the correlation was determined.
    a. This step is valuable when there are regions within the 3-D volume that are not pertinent to the analysis. In this particular case, regions of air outside the actual compact needed to be eliminated from the correlation.
    b. By applying a correlation to the mask, the local volume pertinent to the analysis is found and provides a basis to normalization of the local volumes.
3. Determine the discrete convolution of f by w.
4. Divide the result of Step 3 by the results in Step 2 voxel by voxel to obtain a spatially resolved packing fraction.

Figure 23a shows a 3-D projection of alumina surrogate particles in a graphitic matrix material. The matrix is composed of graphite flake, resin binders, and graphite particles. Upon close inspection of the outer perimeter, the particles in this region appear to have a significantly higher packing fraction. Figure 23b shows the distribution of local packing fraction within the compact. Figure 23c shows variation within the compact perpendicular to the compaction direction. Figure 23d shows variation in packing fraction along the compaction and radial (vertical and horizontal) directions, respectively.

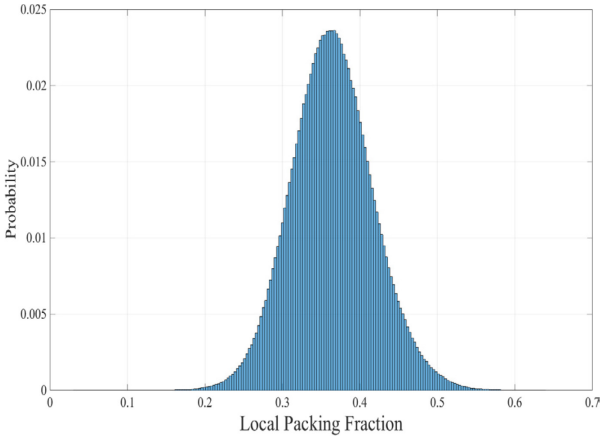

23a

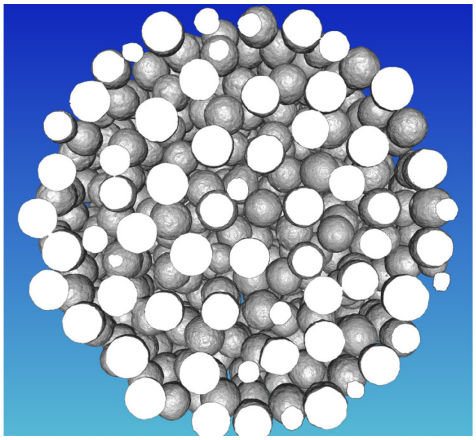

23b

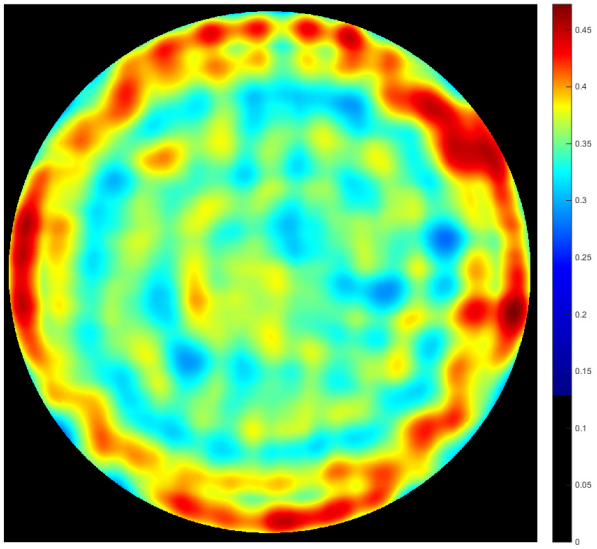

23c

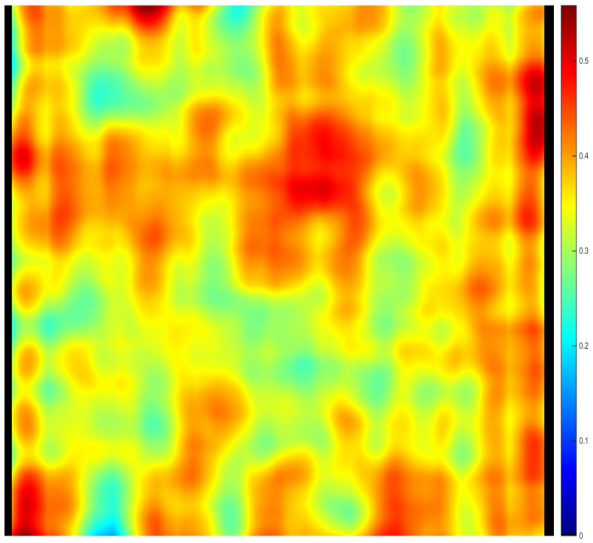

23d

Figure 23. AGR surrogate fuel compact: spatial distribution of packing fraction.

Figure 23 visually shows the results of packing fraction analysis. The packing fraction within the compact appears normally distributed with a mean value of 0.364 and a standard deviation of 0.053 (Figure 23a). On close inspection of Figure 23b, a "rind" of closely packed particles can be seen around the outer rim of the compact. Figure 23c confirms this, but also suggests that the packing fraction roughly appears to oscillate in the radial direction between high and low packing fractions. The high packing fraction in the outer rind has been observed visually and qualitatively noted, but this analysis to the best of our knowledge is the first quantitative measurement of the high packing fraction rind. Finally, Figure 23d may suggest that the particles are not uniformly dispersed in the compaction direction of the compact. These variations could have important implications in terms of the neutron physics and heat transfer within the compact.

3.3.2 Surrogate Tristructural Isotopic Particle

Ideally, TRISO particles should be perfectly spherical. While a great deal of effort has gone into optimizing the complex fabrication process, Figure 22c clearly shows that small deviations do exist from the ideal spherical shape. It is important that asymmetry in the particles is understood and well characterized for the final fabrication conditions since the extreme conditions of an operating HTGR core could exacerbate

the asymmetries over time and ultimately lead to failure. The uniformity and thickness of the various layers are particularly important to understand. Some potential issues may include (1) thermodiffusion of the kernel in a thermal gradient amplified by thinner and thicker regions of particle *longer and shorter paths for heat removal,* as well as other relatively minor issues including (2) non-uniform dimensional change with irradiation and/or temperature in the buffer and inner- outer- pyrolytic carbon layers, and (3) weak regions in the SiC layer leading to failure upon build-up of fission product gases and CO from the interaction of the fuel with carbon.[19]

This section will demonstrate a simple methodology for measuring the radius of the kernel and the thickness of the SiC layer (Figure 24a and 24c) as well as analyze any spatial variation (Figure 24b and 24d). The methodology for determining the kernel radius and SiC thickness are quite similar with only minor variations. For completeness, both are described separately.

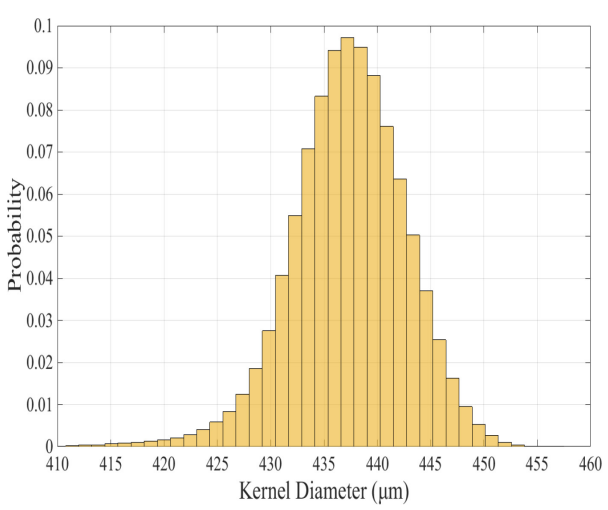

24a

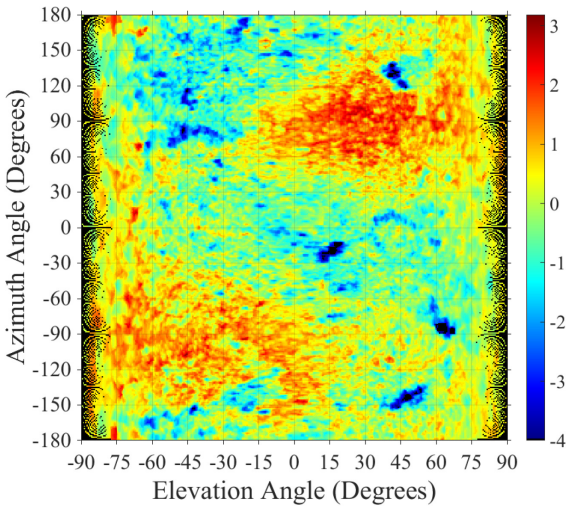

24b

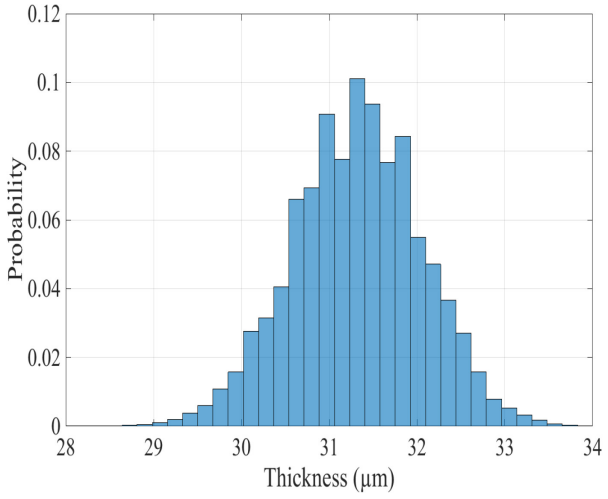

24c

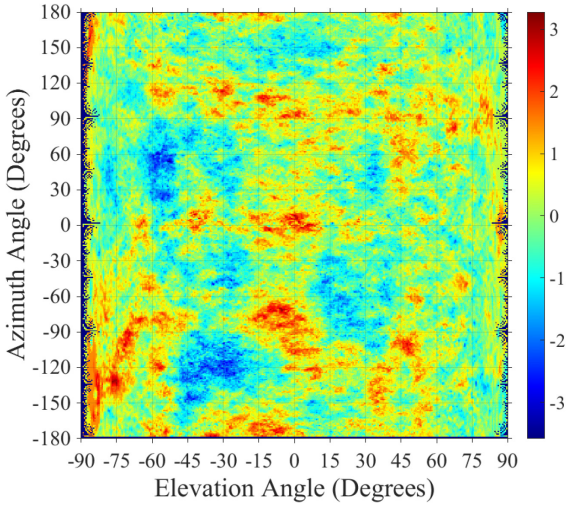

24d

Figure 24. TRISO particle diameter and thickness measurements.

Figure 24a shows a histogram of 3-D kernel diameter measurements extracted from an X-ray CT scan represented by Figure 22c and 21d. Figure 24b shows the variation of kernel diameter as a function of position in 3-D space. The colormap represents the diameter variation in terms of standard deviations

from the mean measurement value, $\mu = 437$ μm and $\sigma = 5$ μm. Figure 24c, similar to Figure 24a, represents the variation in thickness measured for a single TRISO particle $\mu = 31.3$ μm and $\sigma = 0.7$ μm. Figure 24d shows variation in the thickness of the SiC layer as a function of 3-D position. Like Figure 24b, the colormap representing the layer thickness is normalized to standard deviations. A value of +1 means the local thickness is one standard deviation greater than the mean measurement thickness.

To determine the kernel radius:

1. The kernel was first segmented using an automated global threshold (Section 2.1.1)
    a. For distinguishing the similar density buffer and inner pyrolytic carbon layers a global threshold does not properly distinguish between layers. Figure 25 shows a TRISO particle slice after applying a 3-D entropic filter, a basis for texture based segmentation (Section 2.1.3).

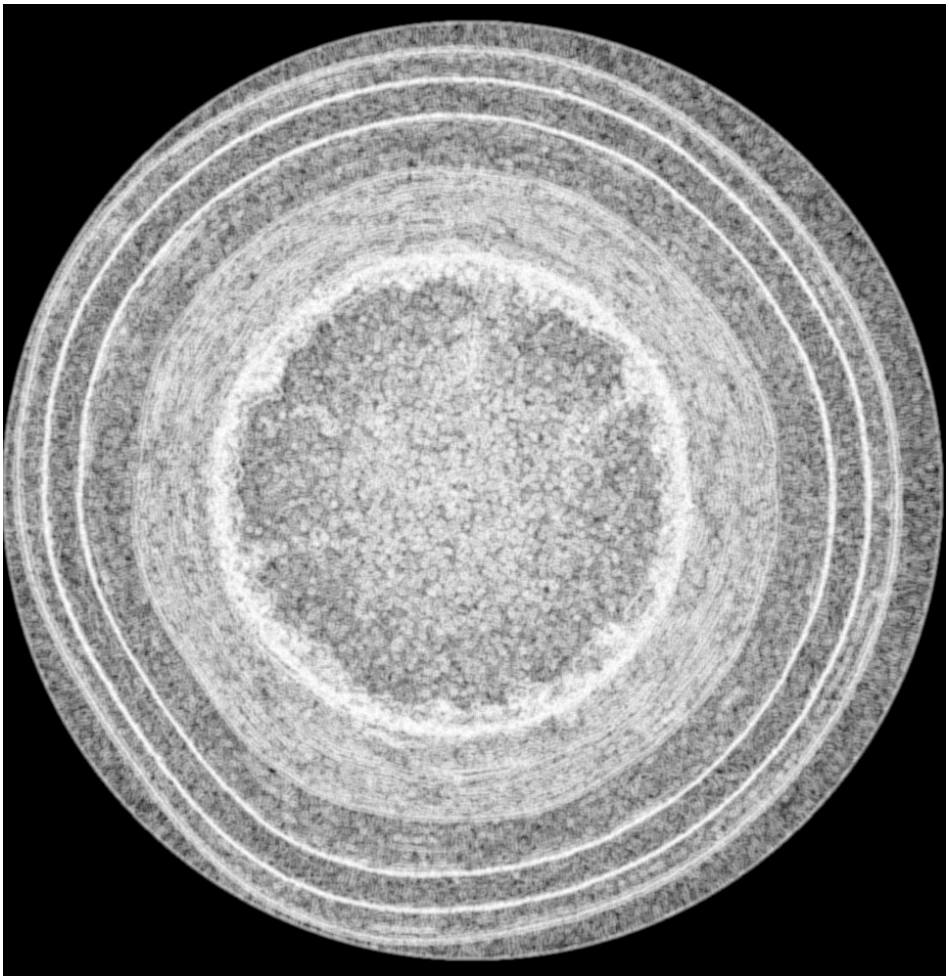

Figure 25. TRISO particle entropic filtering.

Figure 25 shows the results of applying an entropic filter to the X-ray CT slice shown in Figure 22c. Entropic filtering is an alternative method to intensity-based segmentation and may be classified as a texture-based segmentation method.

2. The kernel contained open porosity near the surface and closed porosity within the interior.
    a. Morphological closing (Equation [6]) followed by morphological filling (Equation [10]) removed the porosity and smooth the interface between the kernel and buffer layer.

3. A Euclidean distance transform was determined within the bounds of the kernel volume (Section 2.4).
    a. The kernel centroid was used as the seed point.
4. The outer surface of the kernel was extracted using morphological boundary extraction (Equation [7])
    a. Indices of boundary voxels were extracted using a search algorithm.
5. The Euclidean distances of the boundary voxels correspond directly to the radius of the kernel.

To determine the SiC layer thickness:

1. The layer was segmented using a global threshold algorithm (Section 2.1.1).
2. Small holes were removed using a morphological filling (Equation [10]).
3. Inner and outer surface were extracted using morphological boundary extraction (Equation [7]).
4. A connected component algorithm was used to distinguish between the inner and outer boundary voxels.
5. A Euclidean distance transform was determined for the volume seeded at the inner boundary voxels
6. The Euclidean distances at the outer boundary of the SiC layer are equivalent to the locally measured layer thickness.

To determine spatial variation of measurements:

1. Coordinates of relevant boundaries were determined relative to the kernel center.
2. Position vectors were transformed from Cartesian to spherical.
    a. This was done to reduce dimensional degrees of freedom from 3 to 2.
3. Values were tabulated similarly to binning for a histogram and plotted (Figure 24b and 24d).

3.4 Nuclear Graphite

High purity graphite manufactured for the qualification of reactor grade graphite in the next generation of HTRs is of significant interest to the ART program for application in the next generation of HTRs. In HTRs graphite is used as a moderator, reflector, and high-temperature structural component. Volumetrically, graphite accounts for the majority of an HTR core, thus its performance is vitally linked to the reactors long-term performance. Under the extreme materials environment of an HTR, the reactor lifetime is limited by the phenomena of irradiation-induced creep in permanent graphite blocks within the core. Irradiation-induced creep occurs under the simultaneous application of high temperatures, neutron irradiation, and applied stresses within a graphite component. Significant internal stresses within the graphite component can arise from a second phenomenon, irradiation-induced dimensional change, where graphite component physically changes: first by shrinking and eventually by expanding as greater levels of irradiation dose are achieved. The disparity in component volume change can induce significant internal stresses within the graphite component. Irradiation-induced creep assists in the removal of these large internal stresses, ultimately reducing the probability of crack formation and component failure. Obviously, higher levels of irradiation creep tend to relieve more internal stress, giving a graphite component a longer practical lifetime within an HTR core.

As these phenomena effectively limit the life of an HTR core, it is extremely important that experimental work exists to validate that a particular graphite can be safely used in an HTR core over its lifetime without significant risk of a graphite component failing. The AGC irradiation experiments are currently being conducted to provide this valuable information to potential reactor designers. The AGC experiments were designed to provide an extensive irradiation program to assess irradiation creep within nuclear graphites. The graphites selected for this program encompass multiple nuclear graphite grades, fabrication methods, and carbon feedstock types. In addition, the AGC experiments also provide information regarding thermal, mechanical, and physical property changes in graphite with increasing neutron irradiation dose.

In assessing the data collected from the AGC experiments, it is also critical to develop an understanding of the underlying mechanism(s) controlling graphite behavior under irradiation. Unfortunately, even if a graphite grade was to be qualified today, there is no guarantee that it would be available a decade later to build a reactor. This is primarily due to carbon feedstocks primarily coming from geological sources and variability in the carbon feedstock (even from the same mine but lower in a stratum) having an appreciable effect on the properties of graphites produced by identical processing methods. An example of this includes the current candidate nuclear graphite grade PCEA. PCEA was made to reproduce the historical grade H-451 used in Fort St. Vrain as closely as possible. While PCEA behavior is quite similar to historic H-451, it does not behave identically in terms of its irradiation performance.

Figure 26a is an optical micrograph of cross-sectioned sample of IG-110 graphite. Figure 26b is an optical micrograph of cross-sectioned sample of PCEA graphite. Red is used for both Figure 26a and 26b to highlight large filler particles. Figure 26c and 26d represent tomographic reconstructions of IG-110 and PCEA graphite samples, respectively. Both datasets were collected using μX-ray CT.

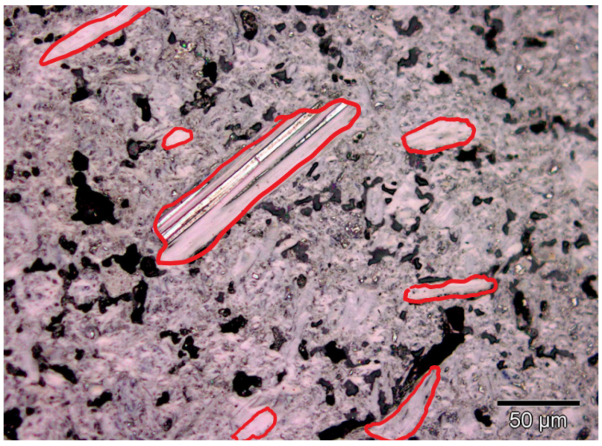

26a

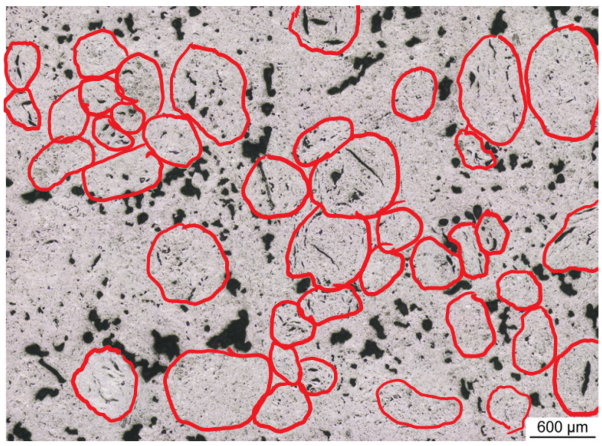

26b

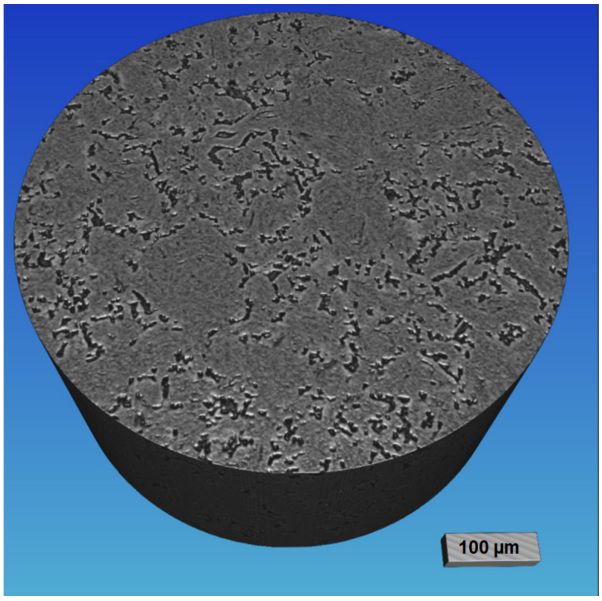

26c

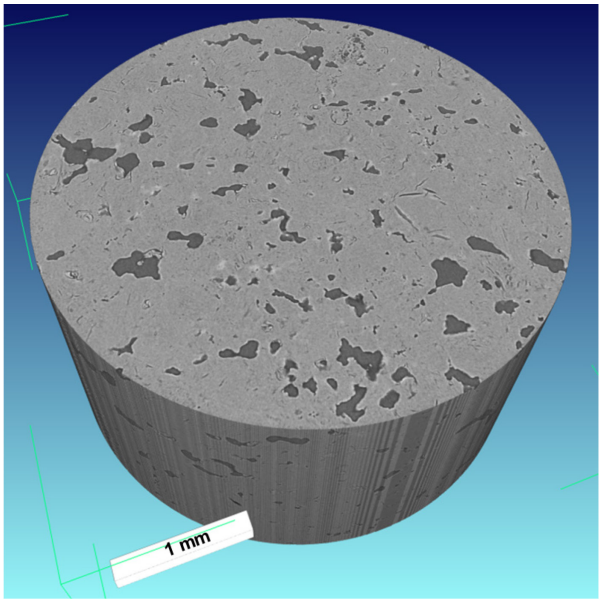

26d

Figure 26. Visual examples of IG-110 and PCEA nuclear graphites.

Nuclear graphites are complex graphite-graphite composites formed from a mixture of calcined filler particles of various sizes and a pitch-like binder-matrix. The mixture is formed by the manufacturer, baked, and then graphitized at temperatures in excess of 2500°C. Optical micrographs highlighting the filler particles in IG-110 and PCEA nuclear graphites are shown in Figure 26a and 26b, respectively. It is quite apparent from these optical micrographs as well as the µX-ray CT reconstructions shown in Figure 26c and 26d that nuclear graphites are by nature highly porous (~17–20% porosity).

The porosity is inherent to the manufacturing process and exists as a complex network of interconnected macroporosity (≥50 nm), mesoporosity (≥2 nm, <50 nm), and microporosity (<2 nm). The complex pore structures of nuclear graphites in turn influence the resulting bulk properties ultimately of interest to an HTR designer. To better understand differing properties between graphite grades as well as changes in performance due to environmental factors such as irradiation and oxidation the pore, structure of nuclear graphites can be assessed non-destructively via X-ray CT. The subsections below describe multiple methodologies for quantitatively assessing various aspects of the pore structure within various nuclear graphites.

3.4.1 Quantitative Assessment of Pores Using Geodesic Tortuosity Mapping

As stated previously, the pore structures of nuclear graphites are quite complex. The pore structure of most nuclear graphites is quite large (~17–20% porosity by volume), they exist across several orders of magnitude in length, and the pore structures are highly interconnected (see Figure 26c and 29b). The interconnectivity especially can make quantitative analysis of the graphite pore structures quite complex simply because there is actually only one large object (the interconnected pore) rather than a discrete number of objects to characterize.

One relatively easy quantitative metric to describe how the pore structure winds through graphite is called geodesic tortuosity. Geodesic tortuosity is essentially a geodesic distance normalized to the Euclidean distance between the corresponding endpoints. For highly porous interconnected pores structures such as those existing within nuclear graphites, defining a value or distribution of tortuosity can be a useful quantitative description of the pore structure in terms of its overall shape and alignment.

The calculation of geodesic tortuosity is directly related to the geodesic distance transform discussed in Section 2.4. The exact value of geodesic tortuosity can be heavily influenced based upon how the user calculates resulting value. The values presented below correspond to the shortest path between two parallel user defined surfaces normalized by the Euclidean distance between those two surfaces.

A tortuosity map can be calculated for a given pore structure as follows:

1. Determine seed planes (designated as SP 1 and SP 2 below)
    a. For a binary representation of graphite this could ideally be the first and last image in a 3-D tomographic stack, SP 1 and SP 2, respectively.
    b. Recall, from Section 2.4, that distance transforms require seed locations for propagation. The authors prefer to use an accurate multi-stencil fast marching algorithm.
2. Calculate distance transform using SP 1.
    a. Account for numerical round off error.
3. Calculate distance transform using SP 2.
    a. Account for numerical round off error.
4. Add both distance transforms together and divide by the Euclidean distance between the two seed planes.

The result of step four can be interpreted as the shortest geodesic distance to pass from SP 1 through the voxel of interest to SP 2. Figure 27a shows the 3-D geodesic tortuosity map resulting for a small sample of PCEA. PCEA is an extruded graphite grade and the geodesic tortuosity map reveals a semi-quantitative view of the alignment of porosity within the grade. For PCEA, there are large, relatively straight pores, aligned nearly perpendicular to the extrusion direction. These pores have a very low tortuosity. There are also a number of pores branching off the large straight pores. They are far more tortuous and appear to have very little preferred alignment. These pores consequently have a much higher tortuosity. This is quantitatively described in Figure 27b.

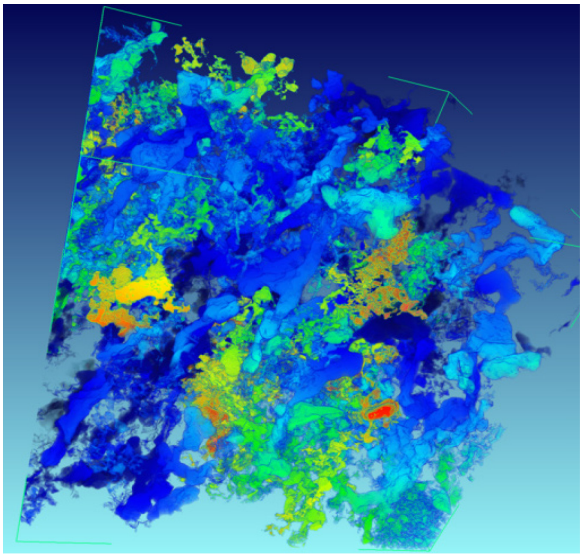

27a

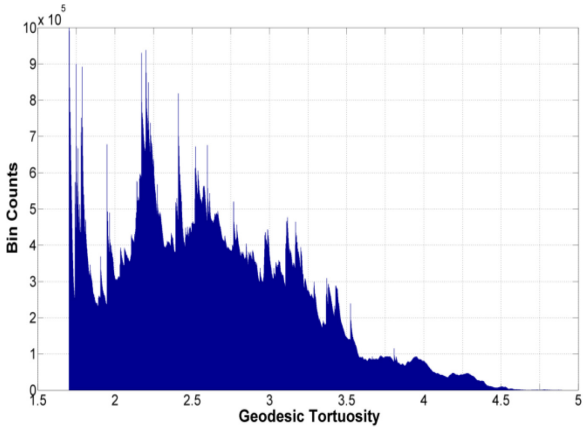

27b

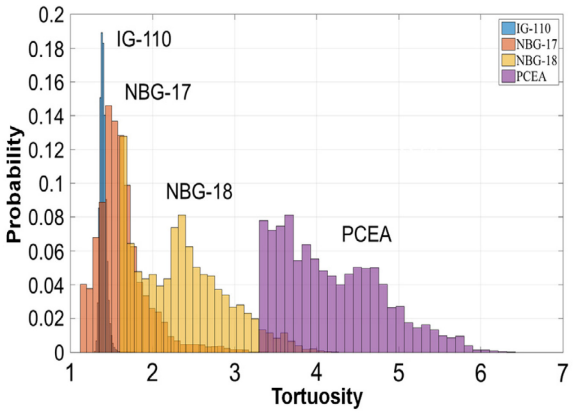

27c

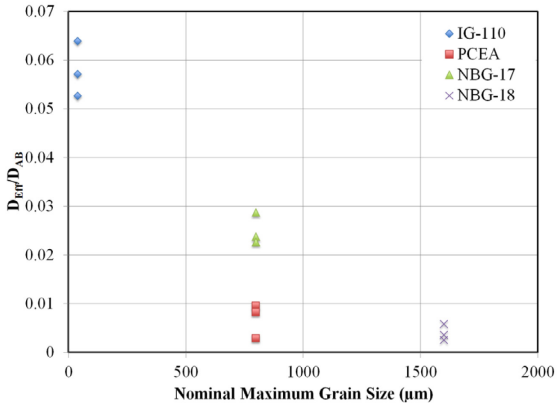

27d

Figure 27. Geodesic tortuosity of nuclear graphites.

Figure 27a is a visual representation of the geodesic tortuosity throughout the open pore structure of the PCEA. Figure 27b corresponds directly to the values represented by a false color map in Figure 27a. The false coloring in Figure 27a is representative of the local value of tortuosity within the pore structure. Dark blue represents the lowest tortuosity, approaching 1, while pores falsely colored red represent tortuosity values approaching 5. The color map used is a standard jet color map. The physical volume represented is roughly $5 \times 5 \times 5$ mm^3. Figure 27c shows tortuosity distributions for various graphite grades. Figure 27d estimates effective diffusivity via Equation 13.

Figure 27c shows typical distributions of tortuosity found within several graphite grades. The shape and average value appears to be correlated, at least indirectly, by the nominal grain size of the graphite specified by the manufacturer. In general, this analysis indicates the mean tortuosity and range of tortuosity values increases with an increase in the nominal grain size. There are exceptions as indicated by the histograms shown for PCEA and NBG-17. Both have a maximum nominal grains size of 800 µm but significantly different tortuosity values. This suggests that the fabrication process strongly influences the graphite microstructure.

Finally, calculations of the geodesic tortuosity can be used to estimate the effective diffusion coefficient of a gas passing through a porous material using Equation (13), where D_{AB} is the binary diffusion coefficient of a gas pair, ε, is the open porosity, σ is a constriction factor, and τ represents the geodesic tortuosity. When combined with experimental diffusivity data an estimated value based on geodesic tortuosity can provide some insight into the relative importance of macropore diffusion (compared to Knudsen diffusion) within a particular graphite. In general, the effective diffusivity decreases with increasing grain size (Figure 27d). Similar to the tortuosity distributions shown in Figure 27c, there is some dependence on the shape and alignment of the porosity as well.

$$D_{Eff} = \frac{D_{AB}\varepsilon\sigma}{\tau^2} \tag{13}$$

3.4.2 Assessing Macropore Evolution Under Uniform Oxidation

In addition to neutron irradiation effects, the oxidation of graphite in an extreme accident scenario could degrade the structural integrity of graphite components. Although accident scenarios are extremely unlikely, understanding the effects of acute oxidation of graphite structural components is vital to predicting the resulting degradation of a graphite component due to oxidation. Prediction of the oxidation rate of nuclear graphite is complicated by several factors, including complex gas-solid reaction kinetics, multiple paths for gaseous mass transport to occur, and the evolution of pore structure with oxidation (depicted in Figure 28). The evolving pore structure gradually changes parameters, such as pore volume, available surface area, and effective mass diffusivity, which control the measured rate of oxidation, thus the apparent rate of oxidation changes with the evolution of pore structure. These parameters can be quite difficult to measure in a static system much less a dynamic time-dependent system, which the estimation of such microstructurally dependent factors are quite valuable.

Figure 28 shows a small graphite cube approximately 5 mm in length with increasing levels of oxidation. Oxidation was simulated with an isotropic morphological erosion of the open porosity. Each figure shows the exterior volume as well as three slices from the x, y, and z planes intersecting at the cube center. The conversion levels for Figures 28a–f are nominally 0, 15, 30, 50, 60, and 70%, respectively.

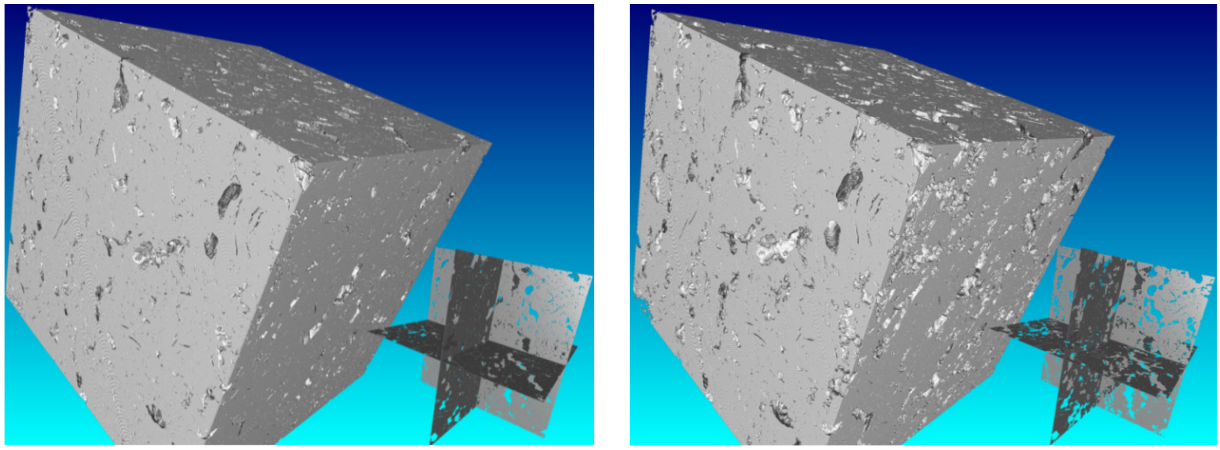

28a

28b

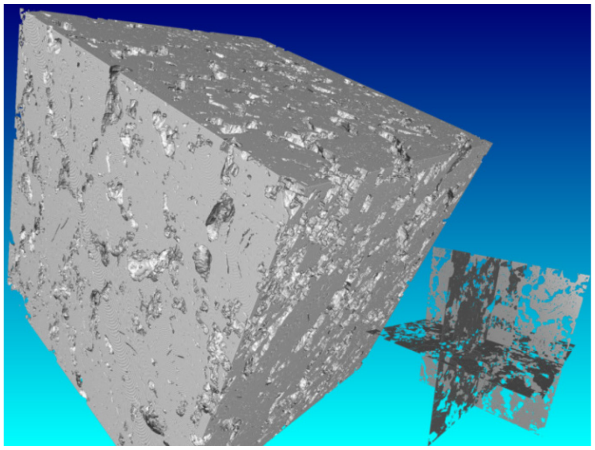

28c

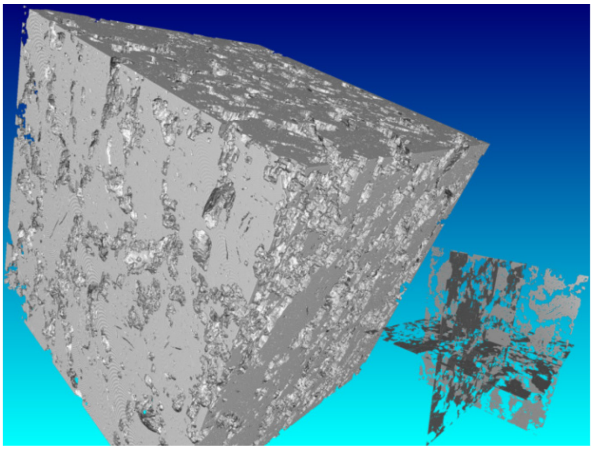

28d

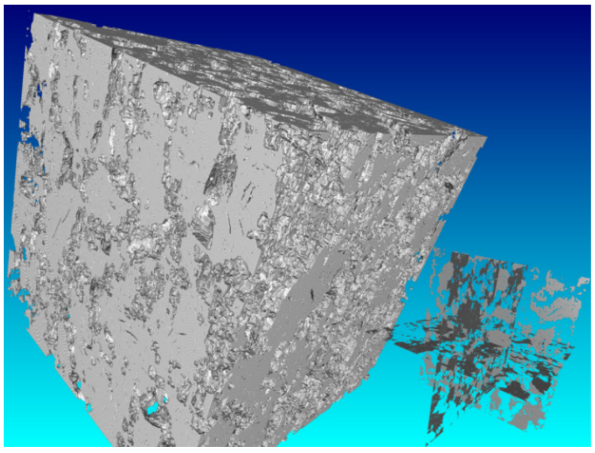

28e

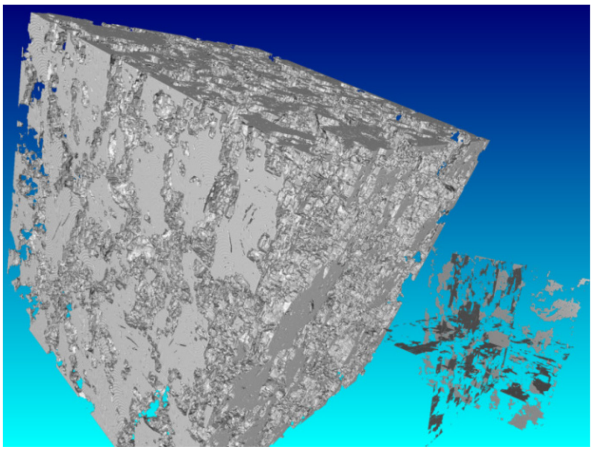

28f

Figure 28. Nuclear graphite and the modelled erosion of the microstructure.

Performing an artificial uniform oxidation of the porosity within a 3-D representation of a particular graphite can provide some preliminary understanding of how a pore structure is expected to evolve with continued oxidation. This can easily be accomplished by combining basic concepts discussed in Section 2 of this report. The procedure is outlined below.

1. Porosity must be segmented (Section 2.1)
    a. Automated global threshold routine is well suited for nuclear graphite (Section 2.1.1)
        (1) Little to no preprocessing is needed if a high quality scan was collected
    b. Represent pores as 0 and graphite material as 1.
2. Pad volume in all three dimensions.
    a. The pad only needs to be one voxel thick.
    b. All pad voxels should have a value of 0.
3. Apply connected components algorithm to padded volume (Section 2.2). Extract the indices of the largest pore.
    a. The largest pore is equivalent to the open porosity available for oxidation.
    b. Create a new volume equivalent in size to the padded volume.
        (1) All voxels should have a value of 1 initially.
    c. Replace values corresponding to indices of largest pore with 0.
    d. Remove pad layer.
4. Apply morphological erosion to graphite material (Section 2.3.1, Equation [3]).
    a. B from Equation (3) should be a $3 \times 3 \times 3$ matrix of ones
    b. Boundaries should be treated as mirrors.

The volume resulting after Step 4 in the above procedure is roughly equivalent to uniformly oxidizing away a layer of graphite one voxel thick anywhere oxygen can penetrate into the sample. By iteratively applying Steps 2–4 the pore structure can be estimated at various levels of oxidation. Once Step 3 is accomplished, the modified volume can be used to estimate parameters, such as total open porosity, surface area, and geodesic tortuosity as a function of oxidation (Figure 29). The percent of open porosity in the graphite volume is simply determined by dividing the total number of voxels with a value of zero after Step 3 by the total number of voxels.

Extracting estimates of the surface area of open porosity can be estimated in a number of ways, the authors personally prefer to use a discrete form of the Cauchy-Crofton theorem as its implementation is relatively inexpensive from a computational standpoint. Essentially this method determines surface area by counting the number of intersects made by a large number of lines with the objects surface, a relatively simple task, and then assigns each intersection an area based on the orientation of the line in 3-D space. The calculation of geodesic tortuosity and indirectly effective diffusivity was discussed in Section 3.4.1.

As stated previously, the simulated evolution of pore structure can provide preliminary estimates of how macroporosity evolves within a particular graphite. It should be noted that this analysis is limited in two respects: (1) it does not have the resolution to resolve meso- and micro- porosity that strongly influences each graphite grade's apparent oxidation rate, and (2) it implicitly assumes all surfaces are equally important in terms of oxidation potential, which is a poor assumption on the atomic length scale. While these measurements have value, their direct use for interpreting the oxidation of graphite must be carefully considered.

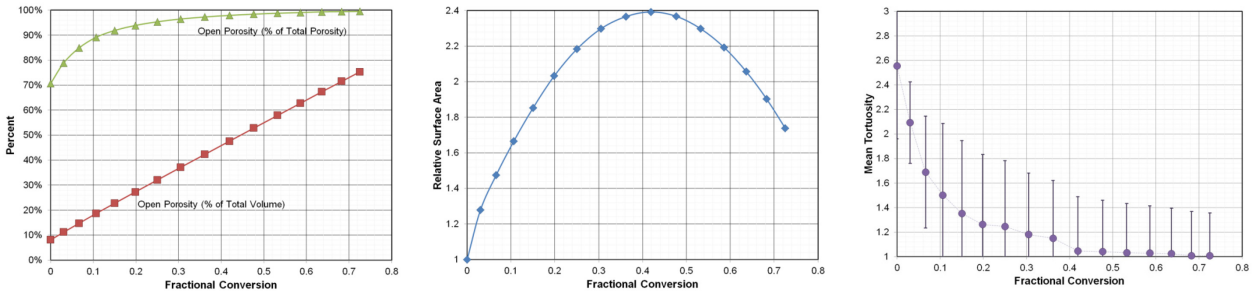

29a 29b 29c

Figure 29. Quantitative analyses of nuclear graphite as a function of simulated oxidation.

Figure 29 plots the quantitative analyses performed on a 5 × 5 × 5 mm^3 sample volume PCEA graphite. Figure 29a–c plot the evolution of open and total porosity, relative available surface area, and mean tortuosity, respectively, against fractional conversion of graphite. Fractional conversion is simulated by morphological erosion of the graphite.

3.4.3 Extracting Branches in Highly Interconnected Pore Structures

Figure 30a represents a 3-D X-ray tomography scan of fine grain nuclear graphite IG-110 scanned with a resolution of approximately 600 nm. The scan detected 13.6% porosity by volume, a little over half of the total porosity found within this nuclear grade (remainder is meso- and microporosity). Of the 13.6% porosity detected, >85% of it was interconnected (Figure 30b). Pore segmentation and representation as a binary volume substantially filters the total amount of information, but as can be seen from Figure 30b, the amount of information available even for the single largest pore within a graphite can be quite overwhelming.

So far the examples shown in Section 3 have focused on analyzing various “well-defined” features of individual objects of interest. For the complex pore structures of nuclear graphites, this is not easily accomplished with the techniques discussed so far in Section 3. The pore structure needs to be filtered further. For nuclear graphites, the pore structure is further distilled a network of primary branches/pathways through the pore structure (Figure 30c), which have varying degrees of branching themselves (Figure 30d). This method is highly reliant initially on the skeletonization of the pore structure. The procedure for determining primary branches along a given direction in a pore structure is outlined below and visually illustrated in a 2-D example with Figure 31.

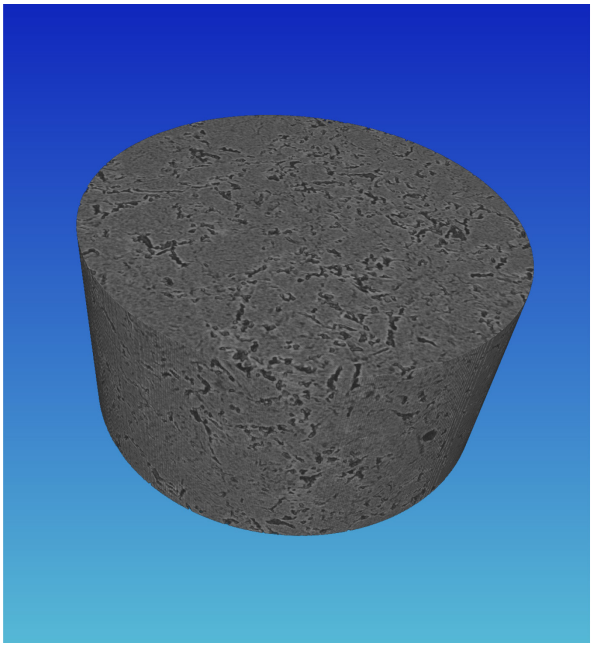

30a

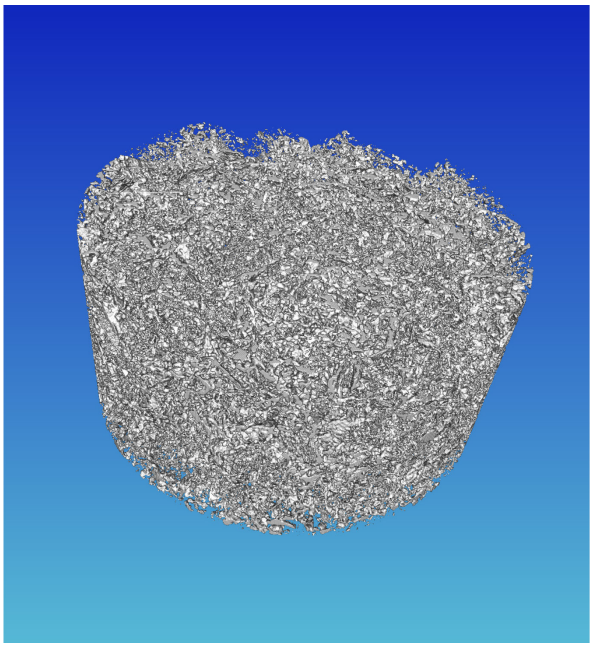

30b

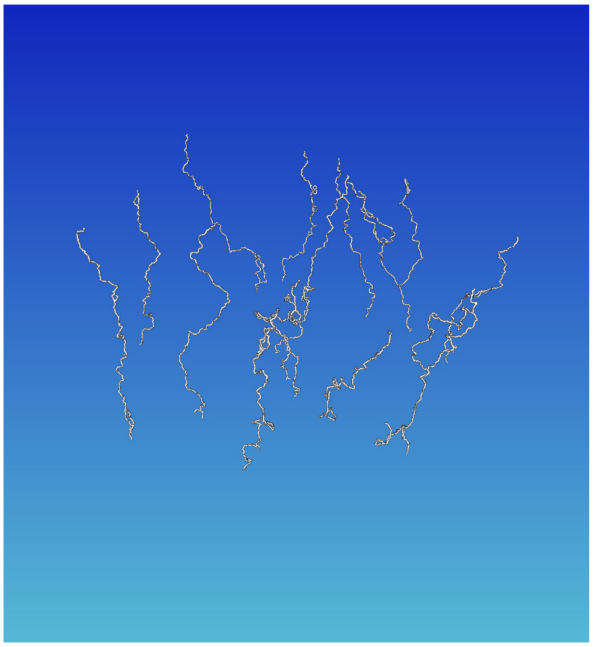

30c

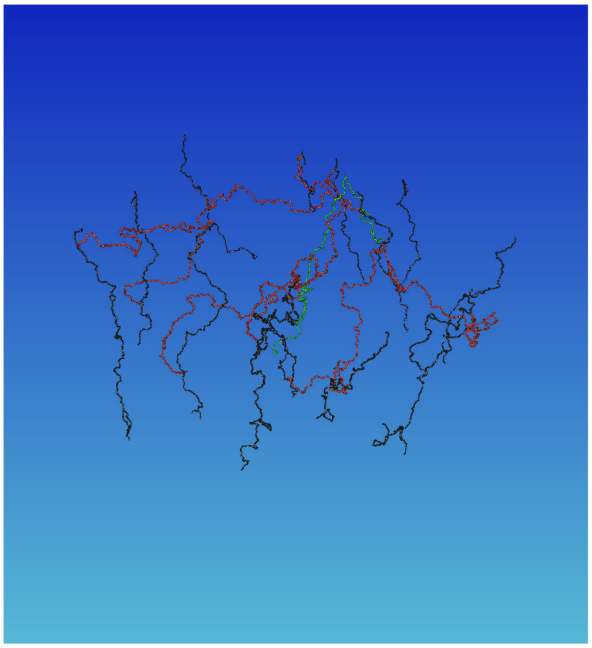

30d

Figure 30. Reduction of pore structure information to a skeletal backbone.

Figure 30a is a visual representation of fine grade graphite IG-110. Figure 30b corresponds to the single-largest pore segmented within the volume represented in Figure 30a. Figure 30c represents the primary pathways to traverse through the segmented pore structure in Figure 30b. Figure 30d shows the secondary branches (red) of one primary branch (green) to other primary branches (black). The analyzed volume was cylindrical (shown in Figure 30a) with a length of 580 µm and a diameter of 580 µm. The voxel size was 600 nm.

1. Isolation interconnected porosity.
    a. Segmentation porosity from initial data volume (Section 2.1).
        (1) A global threshold is adequate for most graphite X-ray CT scans (Section 2.1.1).
    b. Apply connected components algorithm to extract the largest pore (Section 2.2).
2. Skeletonization of pore structure (Section 2.5).
    a. Parasitic branches should be removed via morphological pruning (Section 2.3.2).
        (1) A 3-D example of a skeleton before and after pruning is shown in Figure 18.
3. Determine the geodesic distance map (Section 2.4).
    a. Procedure is nearly identical to that discussed in Section 3.4.1 with the exception that the resulting map does not need to be normalized to the distance between seed planes.
4. Morphologically erode the geodesic distance map (Section 2.3.1)
    a. Use a $3 \times 3 \times 3$ voxel kernel of ones.
    b. The value of all zero elements in the distance map should be forced to equal a value greater than the maximum value observed in the volume prior to erosion.
5. Take the difference element-wise between the result of Step 3 and Step 4.
    a. The voxels with a value greater than two cannot be primary branches
6. Use a connected components algorithm to find all possible primary branches (Section 2.2)
7. Define primary branches as the objects from Step 6 that intersect both seed planes used in Step 3.

    The procedure described above can be modified slightly to isolate sub-branches.

Figure 31a is a synthetic 2-D pore structure with a single primary branch (green) and three secondary branches (red). Figure 31b is the geodesic distance map of Figure 31a and represents Step 3. Figure 31c represents the morphological erosion of the distance map in Figure 31b and represents Step 4. Figure 31d shows the result of subtracting Figure 31c from Figure 31b element by element and represents Step 5.

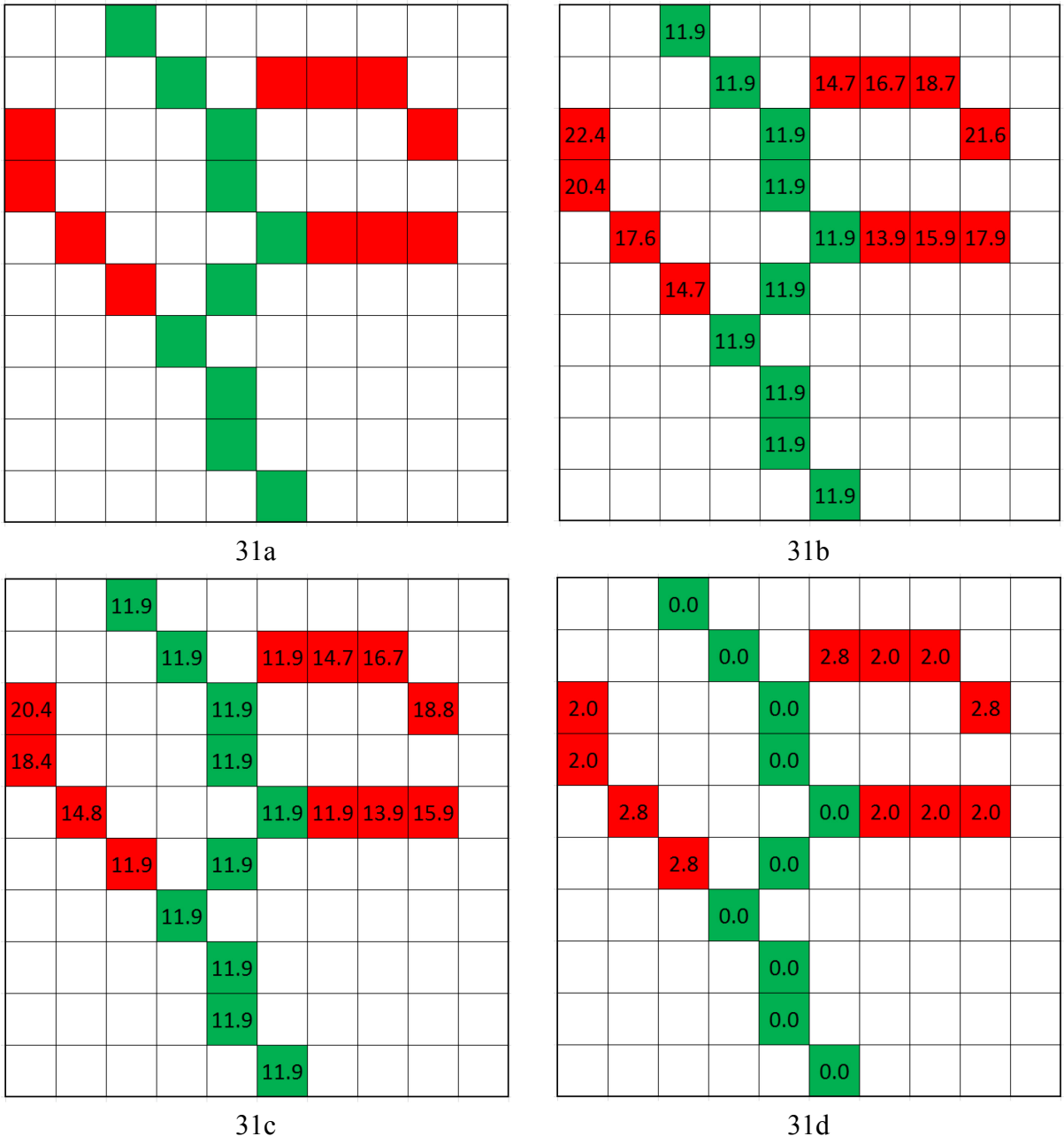

Figure 31. 2-D illustration of primary branch extraction.

3.4.3.1 Using Branching to Extract Additional Quantitative Measurements of the Pore Structure. The branching technique described above has direct application for quantitatively describing the pore structure. For instance, being able to quantify how many sub-branches each branch has (Figure 30c and 30d), could be used as a basis to estimate the fractal dimension of the pore structure. The fractal dimension could then be used to make inferences regarding the nature of the meso- and microporosity.

The following are examples of preliminary results from single X-ray CT scans of IG-110 and PCEA and the results are meant only to show the potential for further development. First, the fracture mechanics of graphite is strongly influenced by the size and number of large pores per unit volume. The current U.S. fracture model requires microstructural inputs, such as quantified through 3-D image analysis, to

accurately predict the fracture strength of candidate nuclear graphites.[18] Figure 32a shows a Voronoi diagram of the 12 primary branches identified for IG-110 in the previous section. On average, each primary branch occupies an area with an equivalent radius of roughly 50 µm, which corresponds to approximately 140 primary pore branches per square millimeter for the IG-110 grade. The number density of primary branches in IG-110 is more than 390 times greater than the number density for PCEA. Thus, the number of potential sites for the initiation of crack growth is significantly larger for IG-110 than it is for the PCEA grade.

The branched structure resulting from Section 3.4.3 can be used as a basis to determine the pore size of different branches in a graphite volume. Figure 32b shows the size distribution of a single primary pore branch of PCEA, while Figure 32c shows how three different primary branches vary in size with length. The mean pore size, from Figure 32b, is approximately 35 µm. From Figure 32c, the mean pore size does not appear to vary significantly between the three tabulated primary pore branches, but does appear to oscillate somewhat between larger and smaller pore sizes.

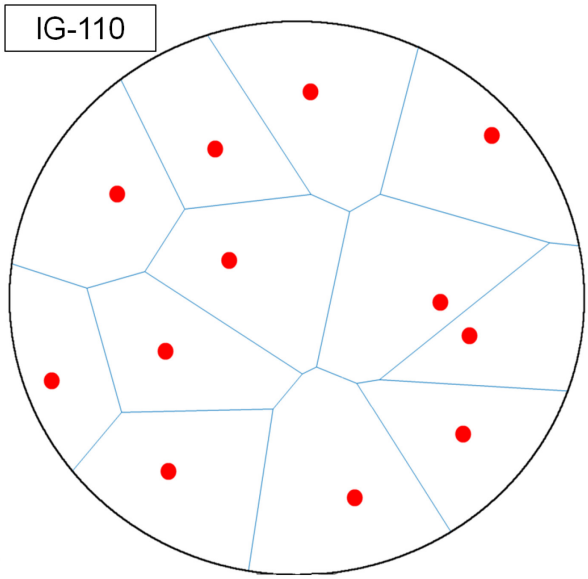

32a

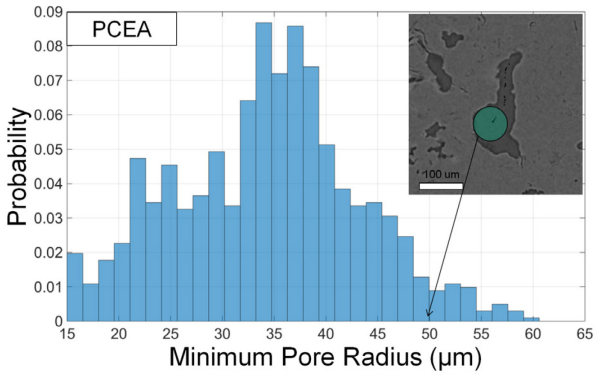

32b

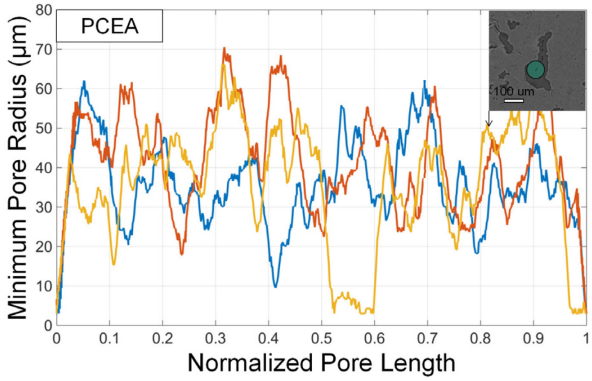

32c

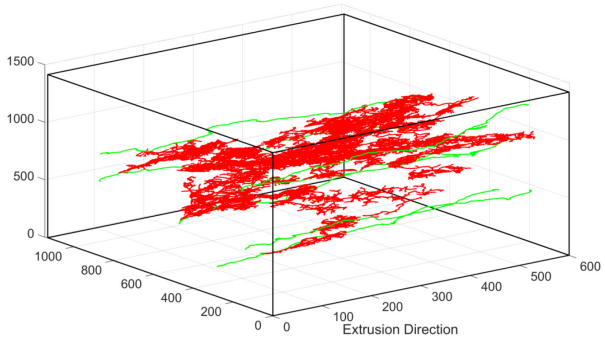

32d

Figure 32. Example quantitative analyses utilizing the methodology from Section 3.4.3.

Figure 32a is a Voronoi diagram of the primary pore branches for IG-110 shown in Figure 30c. The black circle around the perimeter has a diameter of 580 μm. Figure 32b is a histogram representing pore size in a single primary branch of PCEA. The pore size is represented here as the length from the skeletal position of the branch to the pore surface. Figure 32c represents a changing pore size along the lengths of three primary pore branches for PCEA. Figure 32d shows primary (green) and secondary (red) branches for PCEA graphite along the extrusion axis.

Finally, branching can be used to further break down the tortuosity analysis from Section 3.4.1. This is important to help understand the role different branches may have on the effective diffusion rate of gases into a specific graphite microstructure during oxidation. In PCEA for example, the primary branches are most likely the major route by which oxygen can penetrate deep into the structure, but these pores are rather large and the density of active sites as a function of path length for oxygen reaction will be lower. The majority of the reactive surface area is contained within higher-order sub-branches of the pore structure and the effective rate of oxygen transport to these pores will be much more important for graphite oxidation. For the volume of PCEA represented in Figure 22a, the volume averaged tortuosity was 1.45 with a standard deviation of 0.6. Extracting tortuosity values only from regions within primary pore branches, the mean tortuosity is 1.16 with a standard deviation of 0.05. For secondary branches, the mean tortuosity is 1.70 with a standard deviation of 0.46 implying that most oxidation will occur in these secondary branches, which is what is observed experimentally.

The pore size determined for Figures 31b and 31c is a minimum pore radius. The method used for this pore size determination artificially dilates a sphere centered at a particular point on a pore branch until it touches the surface of a pore. This method is relatively simple to implement and computationally inexpensive, but as seen from the insets of Figures 31b and c, it may not be a highly accurate description of pore size. Work is currently underway to more accurately determine pore size as well as determine local orientation of a pore by using geometric spatial transforms to obtain local pore cross-sections orthogonal to the local tangential vector of a pore branch. This will be extremely valuable in determining irradiation induced creep strain and pore generation during tertiary creep in graphite.

4. CONCLUSIONS

Scientists and engineers in the field of materials will always seek to understand a materials structure to predict and understand its behavior and develop new or “better” materials. Three-dimensional image analysis can be a powerful quantitative tool in the field as it provides physical measurements of microstructural features without the restrictive assumptions bounded by feature examination in 2-D. While the application of 3-D analysis of materials is beginning to gain momentum in some areas of materials research, the authors believe a majority of the research community is not aware of the great potential 3-D image analysis can offer. This report was written in part to increase awareness of the powerful quantitative capabilities of image analysis for microstructure characterization for the materials research community in general, but more specifically for those in the field of nuclear materials research.

After a brief introduction to image analysis in Section 1, Section 2 covered several basic concepts, principles, and analysis tools commonly used in image analysis. Section 2 is intended to give the reader an elementary understanding of the basic steps and concepts used in more advanced 3-D materials applications. The reader interested in pursuing the subject matter in more detail is encouraged to consult established texts on 2-D image processing and analysis.[14,15,16,17]

Section 3 took the concepts discussed in Section 2 and used them to demonstrate actual quantitative measurements of real 3-D microstructures collected via μX-ray CT. This section provided the reader a brief overview of a few of the many types of quantitative measurements that can be extracted from 3-D data sets along with the basic steps needed to extract the information. Since specialists in the field of nuclear materials were a target audience, three materials from different INL program were selected to illustrate quantitative image analysis: the TREAT LEU conversion program (Section 3.2), the ART AGR Fuels Program (Section 3.3), and the ART Graphite Research and Development Program (Section 3.4).

Each subsection provided a short summary of the materials application and brief explanation regarding the value of the 3-D analysis. As current INL expertise in 3-D image processing and analysis evolved out of the ART Graphite Research and Development Program, Section 3.4 gives more detail than Sections 3.2 and 3.3 regarding the importance of the quantifications and the usefulness of the quantified values for developing various predictive models.

5. REFERENCES

1. Karacan, C.O., "An effective method for resolving spatial distribution of adsorption kinetics in heterogeneous porous media: application for carbon dioxide sequestration in coal," *Chem Eng Sci*, May 2003, Vol. 58, pp. 4681–4693.
2. Bera, B., S. K. Mitra, D. Vick, "Understanding the micro structure of berea sandstone by simultaneous use of micro-computed tomography (micro-CT) and focused ion beam-scanning electron microscopy (FIB-SEM)," *Micron,* 2011, Vol. 42, pp. 412–418.
3. Manickam, S. S., J. Gelb, J. R. McCutcheon, "Pore structure characterization of asymmetric membranes: Non-destructive characterization of porosity and tortuosity," *J Membrane Sci*, 2014, Vol. 454, pp. 549–554.
4. Kenney, B., M. Valdmanis, M. Baker, J. G. Pharoah, K. Karan, "Computation of TPB length, surface area and pore size from numerical reconstruction of composite solid oxide fuel cell electrodes," *J Power Sources*, 2009, Vol. 189, pp. 3592–3603
5. Gommes, C. J., A-J. Bons, S. Blacher, J. H. Dunsmuir, A. H. Tsou, "Practical methods for measuring the tortuosity of porous materials from binary or gray-tone tomographic reconstructions," *AIChE Journal*, 2009, Vol. 55 No. 8, pp. 2000–2012.
6. Peurega, C., D. Jeulin, "Estimation of tortuosity and reconstruction of geodesic paths in 3-D Image," Anal Stereol, 2013, Vol. 32, pp. 27–43.
7. Luo, L., H. Lin, "Lacunarity and fractal analyses of soil macropores and preferential transport using micro-x-ray computed tomography," *Vadose Zone J*, 2008, Vol. 8, pp. 233–241.
8. Suuronen. J-P., A. Kallonen, M. Eik, J. Puttonen, R, Serimaa, H. Herrmann, "Analysis of short fibres orientation in steel fibre-reinforced concrete (SFRC) by x-ray tomography," *J Mater Sci,* 2013, Vol. 48, pp. 1358–1367.
9. Matsuzaki, K., N. Shiazono, N. Kasagi, "Three-dimensional numerical analysis of mixed ionic and electronic conducting cathode reconstructed by focused ion beam scanning electron microscope," *J Power Sources*, 2011, Vol. 196, pp. 3073–3082.
10. Gunda, N. S. K., W-W. Choi, A. Berson, B. Kenney, K. Karan, J. G. Pharoah, S. K. Mitra, "Focused ion beam-scanning electron microscopy on solid-oxide fuel-cell electrode: Image analysis and computing effective transport properties," *J Power Sources,* 2011, Vol. 196, pp. 3592–3603.
11. Cooper S. J., D. S.,\ Eastwood, J. Gelb, G. Damblanc, D. J. L. Brett, R. S. Bradley, et al., "Image based modelling of microstructural heterogeneity in $LiFePO_4$ electrodes for Li-ion batteries," *J Power Sources*, 2014, Vol 247, pp. 1033–1039.
12. Shearing P. R., L. E. Howard, P. S. Jorgensen, N. P. Brandon, S. J. Harris, "Characterization of the 3-dimensional microstructure of a graphite negative electrode from a Li-ion battery," *Electrochem Commun*, 2010, Vol 12, pp. 374–377.
13. Eastwood D. S., R. S. Bradley, F. Tariq, S. J. Cooper, O. O. Taiwo, et al., "The application of phase contrast X-ray techniques for imaging Li-ion battery electrodes," *Nucl Instrum Methods B*, 2014, Vol. 324, pp. 118–123.

14. Gonzalez, R. C. and R. E. Woods, *Digital Image Processing*, third ed., Pearson Inc., New Jersey, 2008.

15. Soille, P., *Morphological Image Analysis Principles and Applications*, second ed., Springer, New York, 2003.

16. Serra, J. P., *Image Analysis and Mathematical Morphology Volume 2: Theoretical Advances.* London: Academic Press, 1982. Print.

17. Serra, J. P., *Image Analysis and Mathematical Morphology.* London: Academic Press, 1988. Print.

18. Kane J. J., I. J. Van Rooyen, A. E. Craft, T. J. Roney, S. Morrell, "Evaluating quantitative 3-D Image Processing and Analysis as a design tool for low enriched uranium fuel compacts for the transient reactor test facility: A preliminary study," *Nucl Eng Des*, 2016, Vol. 300, pp. 1–11.

19. Lowe T., R.S. Bradley, S. Yue, K. Barii, J. Gelb, N. Rohbeck, J. Turner, P. J. Withers, "Micostructural analysis of TRISO particles using multi-scale X-ray computed tomography," *J Nucl Mater*, 2015, Vol. 461, pp. 29–36.